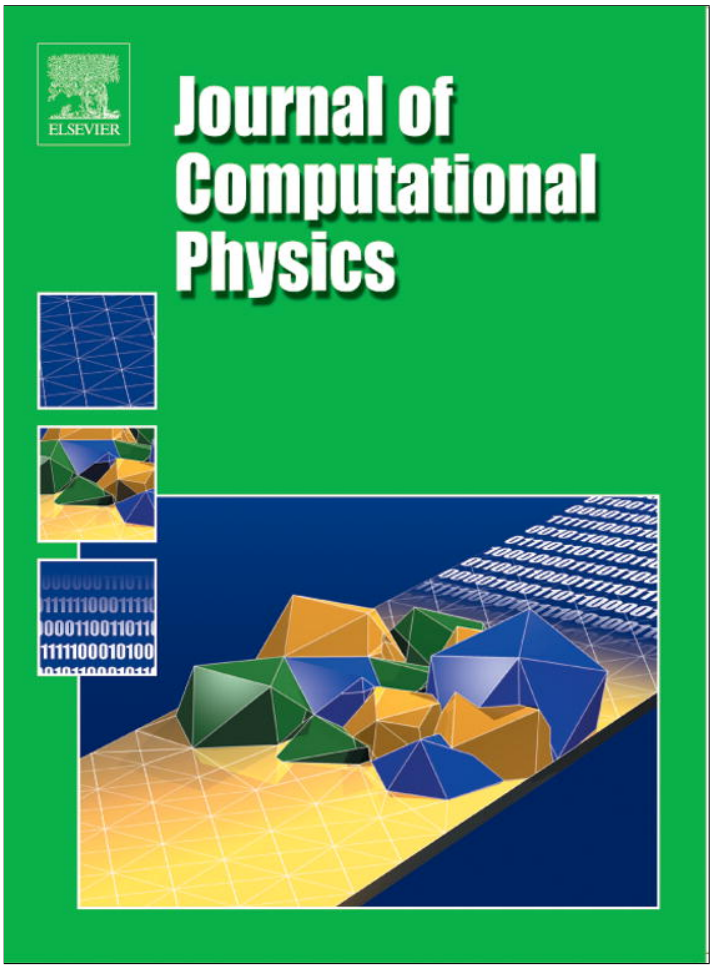

Journal of Computational Physics 253 (2013) 18–49

Contents lists available at SciVerse ScienceDirect

Journal of Computational Physics

www.elsevier.com/locate/jcp

A discrete geometric approach for simulating the dynamics of thin viscous threads

B. Audoly [a,*], N. Clauvelin [a], P.-T. Brun [a,b], M. Bergou [c], E. Grinspun [c], M. Wardetzky [d]

[a] Institut Jean Le Rond d'Alembert, UMR 7190, UPMC Univ. Paris 06 and CNRS, F-75005 Paris, France
[b] Laboratoire FAST, UPMC Univ. Paris 06, Université Paris-Sud and CNRS, Bâtiment 502, Campus Universitaire, Orsay 91405, France
[c] Computer Science, Columbia University, New York, NY, USA
[d] Institute for Numerical and Applied Mathematics, University of Göttingen, 37083 Göttingen, Germany

ARTICLE INFO

Article history:
Received 17 March 2012
Received in revised form 20 June 2013
Accepted 24 June 2013
Available online 8 July 2013

Keywords:
Viscous rod
Bending
Twisting
Rayleigh–Taylor analogy
Viscous coiling

ABSTRACT

We present a numerical model for the dynamics of thin viscous threads based on a discrete, Lagrangian formulation of the smooth equations. The model makes use of a condensed set of coordinates, called the centerline/spin representation: the kinematic constraints linking the centerline's tangent to the orientation of the material frame is used to eliminate two out of three degrees of freedom associated with rotations. Based on a description of twist inspired from discrete differential geometry and from variational principles, we build a full-fledged discrete viscous thread model, which includes in particular a discrete representation of the internal viscous stress. Consistency of the discrete model with the classical, smooth equations for thin threads is established formally. Our numerical method is validated against reference solutions for steady coiling. The method makes it possible to simulate the unsteady behavior of thin viscous threads in a robust and efficient way, including the combined effects of inertia, stretching, bending, twisting, large rotations and surface tension.

1. Introduction

1.1. Context

The flow of thin viscous filaments is relevant to a variety of industrial processes such as the drawing and spinning of polymer and glass fibers [1–3], and to natural phenomena such as formation of Pele's hair by lava ejected at high speed by volcanoes [4]. In art, Jackson Pollock took advantage of the coiling instability of a thin viscous fluid, the paint, impinging a surface, the canvas, to produce a variety of decorative patterns by a fluid-mechanical process [5]. A commonplace version of the same coiling instability is observed when a thin thread of honey is poured on a morning's toast. This steady coiling problem is prototypical of the dynamics of thin threads. Its apparent simplicity has made it appealing to fluid mechanicians for a long time [6,7]; however the various regimes of steady coiling and its non-linear features, such as the coexistence of multiple stable states, have been understood in full details only recently [8–11]. To a large extent, the analysis of steady coiling has been made possible by the availability of numerical simulation: the shape of the thread in the co-rotating frame is stationary, and is given by a non-linear boundary-value problem [9] which has been solved using numerical continuation.

* Corresponding author.
E-mail address: audoly@lmm.jussieu.fr (B. Audoly).

0021-9991/$ – see front matter
http://dx.doi.org/10.1016/j.jcp.2013.06.034

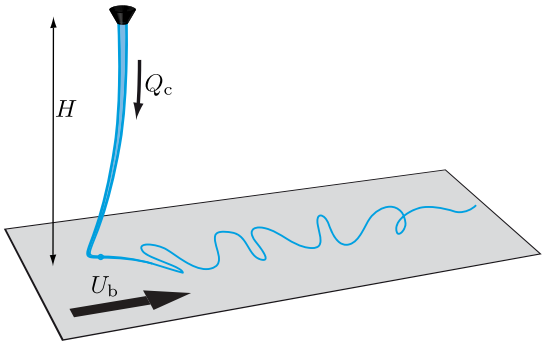

Fig. 1. The fluid-mechanical sewing machine illustrates the complex behavior of thin viscous threads. This sketch of the experiment of [12] shows a thread poured onto a moving belt. The thread traces out a number of possible patterns depending on the fluid properties, the injection volume rate Q_c, the rate of fall H and the belt velocity U_b. This geometry is simulated using our method at the end of the paper in Section 6.2.

In this paper we are interested in the simulation of the unsteady behavior of thin threads, which is far less advanced. As an illustration, consider a recently proposed variant of the coiling problem, similar to Pollock's painting technique, whereby the target surface moves horizontally at a constant velocity, as illustrated in Fig. 1. The relative motion suppresses steady coiling solutions and forces the flow to become unsteady. More than ten different patterns can be produced by varying the lateral velocity of the surface and the fall height [12,13], a number of which have convoluted and intriguing shapes. The patterns are reminiscent of stitch patterns, and the experiment has been coined the 'fluid-mechanical sewing machine'. This experiment illustrates the complex behavior that can result from the dynamics of a thin, perfectly viscous filament. Except for the one presented in this paper, existing numerical methods are unable to reproduce this behavior.

The dynamics of thin threads is governed by the interplay of three local modes of deformation, namely stretching, bending and twisting modes [14,15]. At the global scale, these modes are coupled by geometrically non-linear terms, which makes the resulting dynamics remarkably rich. The main difficulty in simulating the motion of thin threads is that the underlying non-linear partial differential equations are numerically stiff, due to the different length scales at which stretching and bending operate. This paper tackles this difficulty by introducing a careful and well-controlled space discretization. In fact, we introduce a full-fledged *discrete* viscous thread model by extending all the relevant physical quantities, such as strain rates and internal stress, to the discrete setting.

Fluid-mechanical problems involving free boundary conditions can be simulated using refined variants of the marker and cells method, namely the method of [16,17] for 2d viscous flows, and the GENSMAC method [18,19] for 3d viscous flows; more recently implicit schemes coupled with projection methods have been proposed, see e.g. [20]. The present paper is concerned with thin filaments, for which the above methods are not efficient: when the thickness is small compared to the longitudinal length scale, it is beneficial to use dimensionally reduced equations as a starting point for simulations. Thanks to dimensional reduction, the structure of the flow at small scale is solved analytically, which makes it possible to use a simulation grid much coarser than the thickness.

While our simulation method addresses the general non-steady dynamics of a thin thread governed by the combined effects of twist, bending and stretching forces, inertia and large rotations, a number of particular cases have been simulated in the literature. Steadily rotating viscous threads are described by time-independent equations in the co-rotating frame, which have been solved numerically using methods for two-point boundary-value problems [9,11,21]. The dynamics of a viscous string, where both the bending and twisting modes are neglected, has been considered [22]. The periodic folding of a viscous thread or sheet has been considered in a 2d geometry [23,24] where twist does not play any role. By combining the simulation of steady solutions with analytical expansions describing oscillatory perturbations of small amplitude, the stability of both the steady coiling solution [11] and of the catenary-like profile of a dragged thread [25] have been calculated. Many other problems, such as the existence of rotatory folding, the competition between folding and coiling [26], the stitch patterns produced by the fluid-mechanical sewing machine [12] and the loss of stability of steady coiling by precession [27] remain inaccessible to those simulation methods that are based on restrictive assumptions.

In comparison to viscous threads, elastic rods have received a lot of attention, both from the perspective of analysis [28–31] and simulation [32–37]. By the Rayleigh–Taylor analogy [7], the stress in a viscous fluid is identical to the stress in an elastic solid, when the *strain rate* is replaced with the *strain*. This analogy explains the buckling of viscous sheets [38,39], a phenomenon classically associated elastic structures. One can take advantage of this analogy to simulate the dynamics of viscous threads using a simulation tool written for elastic rods [40]; we explored this approach in a conference paper [41]. Here we propose a self-standing implementation of the viscous model.

Stretching is important for viscous threads, even though it is often neglected for thin elastic rods. This is well illustrated by the phenomenon of helical coiling: a thin thread poured from a container onto a fixed obstacle gets stretched by gravity. It remains straight over almost the entire fall height, but bends and twist severely in a small boundary layer near the bottom. Even though the rate of stretching is mild everywhere along the thread, its effect is cumulated over the entire time of descent. As a result, the net stretch is significant, and the thread is much thinner at the bottom.

In one of our recent papers [42], some of us have used the numerical method presented here to set up numerical experiments of the viscous sewing machine; our goal was to get physical insights into this fluid-mechanical problem. We introduced the principles of the numerical method, staying at a very general level and providing no details on how the twist is treated, for instance. The present paper is the first complete description of our numerical method.

1.2. Features of the model

The derivation of dimensionally reduced models for thin viscous filaments has a long history. The equations for thin viscous threads were derived by asymptotic expansion from the equations for a 3d viscous fluids by Entov and Yarin [43]. Their work builds upon the previous analyses of viscous stretching by Trouton [14], and of viscous bending by Buckmaster and co-workers [44,45]. Recent derivations of the equations for thin threads benefit from a clear identification of the mechanical quantities in the 1d model [46], and of the systematic use of Lagrangian coordinates [21]. Asymptotic models accounting for more general constitutive laws have been proposed: the case of a visco-elastic fluid is treated in [47], and a general framework is considered in [48] which can produce a variety of asymptotic models when a specific set of physical effects is considered.

Here we consider the dynamics of a thin filament of an incompressible, purely viscous fluid having circular cross-section, under the action of external forces such as gravity, and internal forces (viscous stretching, bending, twisting, and capillary tension). We consider the 3d problem, and the curvature and kinematic twist of the thread can be comparable to, or smaller than the inverse of the thread's length. Even though the fluid is very viscous, the effect of inertia is considered. The role of inertia is well illustrated by the classical analysis of the pendulum modes of a viscous string, see e.g. [10]: in this almost straight geometry, the flow in the axial direction is typically governed by a small Reynolds number and dominated by viscosity, although the flow in the transverse direction, which is characterized by different length and time scales, is associated with a much larger Reynolds number and dominated by inertia. In general, the local axial and transverse modes get coupled by the curvature of the filament.

1.3. Proposed approach

The main features of our numerical method are the following. It is based on a 1d model obtained by dimensional reduction, which makes it much more efficient than a general-purpose model for 3d viscous flows. We use a Lagrangian grid, making simulation vertices flow along with the fluid; this simplifies the computation of viscous forces which, by the constitutive law, are proportional to the co-moving time derivative of the kinematic twist and curvature. We use a reduced set of coordinates, called the centerline/spin representation, obtained by eliminating two out of three degrees of freedom associated with rotations. Our description of the internal viscous stress includes the three physically relevant contributions of stretching, bending and twisting. The discrete expressions of these forces are derived naturally based on the variational method of Rayleigh potentials. Given the numerical stiffness of the underlying problem, robustness is a central issue. In our numerical scheme, the viscous forces are treated implicitly with respect to the velocity. Together with a careful space discretization, this provides excellent robustness.

The discretization of bending in elastic rods is routinely done using flexural springs at hinges [49], and the extension to viscous bending is straightforward. Discrete twist forces are much less common. Ours make use of a discrete notion of twist based on concepts from discrete differential geometry, and are directly borrowed from our previous work on elastic rods [35].

This paper is organized as follows. In the rest of this section we derive useful identities of geometry and differential calculus. In Section 2 the equations for thin viscous threads are presented in a way that prepares the extension to the discrete setting: the Lagrangian centerline/spin description of motion is introduced and the internal viscous forces and moments are derived from variational principles. In Section 3 the discrete model is presented in close analogy with the smooth case. Section 4 considers time discretization, the treatment of boundary conditions and the coupling of the thread with external bodies. In Section 5, the code is validated against reference solutions for steady coiling. In Section 6, we discuss limitations and perspectives. In Appendices A–D, we provide material that helps building up a physical intuition of our numerical thread model, and demonstrates equivalence with the Kirchhoff equations familiar to fluid and solid mechanicians.

1.4. Mathematical identities and notations

We use underlines for vectors ($\underline{a}$) and double underlines for rank-two tensors such as matrices ($\underline{\underline{a}}$).

Infinitesimal rotations are described as follows. Consider an orthonormal frame $\underline{d}_i(\sigma)$ in the 3d Euclidean space, $i = 1, 2, 3$, which is a smoothly differentiable function of a continuous parameter σ. Its rate of rotation is measured by the Darboux vector $\underline{\Gamma}(\sigma)$, defined as the unique vector such that for any $i = 1, 2, 3$:

$$\frac{\mathrm{d}\underline{d}_i(\sigma)}{\mathrm{d}\sigma} = \underline{\Gamma}(\sigma) \times \underline{d}_i(\sigma). \tag{1}$$

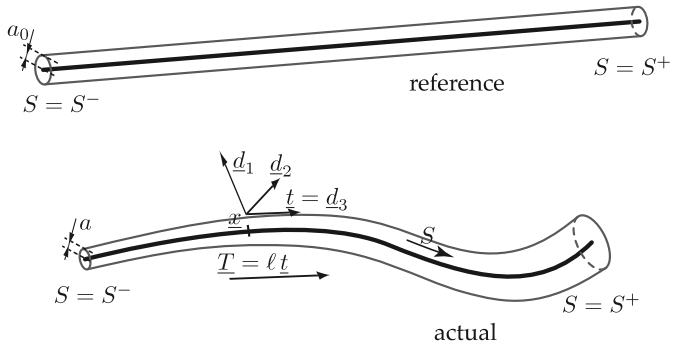

Fig. 2. Reference and actual configuration of the thread.

This definition will be used later with σ replaced by the time t, or the arc length S. An explicit expression for the Darboux vector can be found by singling out any particular vector $\underline{d}_i$ in the triad, say $\underline{d}_3$:

$$\underline{\Gamma}(\sigma) = \underline{d}_3(\sigma) \times \frac{\mathrm{d}\underline{d}_3(\sigma)}{\mathrm{d}\sigma} + \Gamma_3(\sigma)\,\underline{d}_3(\sigma), \tag{2}$$

where $\Gamma_3 = \underline{\Gamma} \cdot \underline{d}_3$ is defined by

$$\Gamma_3(\sigma) = \frac{\mathrm{d}\underline{d}_1(\sigma)}{\mathrm{d}\sigma} \cdot \underline{d}_2(\sigma). \tag{3}$$

This can be checked by inserting Eq. (3) into Eq. (2) and then into Eq. (1).

For any unit vector $\underline{q}$ and for any vector $\underline{a}$, the projection $\underline{P}_\perp$ in the direction perpendicular to $\underline{q}$ is defined by

$$\underline{P}_\perp(\underline{q}, \underline{a}) = (\underline{1} - \underline{q} \otimes \underline{q}) \cdot \underline{a} = \underline{a} - (\underline{q} \cdot \underline{a})\,\underline{q}, \tag{4}$$

where the last term in the right-hand side is the longitudinal projection.

2. Smooth setting: the centerline/spin representation of viscous threads

Thin threads have been simulated using Eulerian variables, see e.g. [11,21]. Equations of motion based on Lagrangian variables have been derived [21], but we are not aware of any simulation method for thin viscous threads based on a Lagrangian grid. This is the approach we explore in this paper. It allows one to simulate the non-steady behavior of thin threads in a convenient way. In this section, we start by deriving the centerline/spin representation of thin threads in Lagrangian variables: this form of the equations of motion is used later to derive the discrete model.

2.1. Reference configuration

The Lagrangian description makes use of a reference configuration. A convenient choice is to use an infinite, circular cylinder of constant radius a_0, as illustrated in Fig. 2. The fluid being incompressible, assume that the mapping between the reference and actual configurations preserves volume.

2.2. Kinematics of centerline

The viscous thread can stretch, and we make a careful distinction between the arc length measured in reference configuration, which is denoted by S, and the arc length measured in actual configuration, denoted by s. We use S as the Lagrangian coordinate: it follows fluid particles. Let t be the time. For any function $f(S,t)$, we denote its spatial derivative using a prime, and its time derivative using a dot,

$$f'(S,t) = \frac{\partial f(S,t)}{\partial S}, \qquad \dot{f}(S,t) = \frac{\partial f(S,t)}{\partial t}. \tag{5}$$

This time derivative is known as a *convected* derivative, and is often written $\dot{f} = \frac{\partial f}{\partial t} = \frac{\mathrm{D}f}{\mathrm{D}t}$ in the Eulerian context.

At time t the centerline of the thread is given by the function $\underline{x}(S,t)$, see Fig. 2. The material tangent of the thread is denoted by $\underline{T}(S,t)$ and defined by

$$\underline{T}(S,t) = \underline{x}'(S,t). \tag{6}$$

Note that this is not a unit vector in general.

Indeed, the norm of $\underline{T}(S,t)$, denoted by $\ell(S,t)$, measures the amount of stretching of the centerline with respect to the reference configuration:

$$\ell(S,t) = \left|\underline{T}(S,t)\right| = \left|\frac{\partial \underline{x}(S,t)}{\partial S}\right|. \tag{7}$$

The unit tangent to the centerline is then defined by

$$\underline{t}(S,t) = \frac{\underline{T}(S,t)}{\ell(S,t)}. \tag{8}$$

In our Lagrangian description, the arc length s in actual configuration is viewed as a secondary quantity. It can be reconstructed by integration of the differential equation expressing the identity $\mathrm{d}s = |\mathrm{d}\underline{x}|$, namely $s'(S,t) = \ell(S,t)$.

The velocity $\underline{u}$ is simply the time derivative of position,

$$\underline{u}(S,t) = \frac{\partial \underline{x}(S,t)}{\partial t}. \tag{9}$$

The rate of change of the stretching strain of the centerline is denoted by d and defined by

$$d(S,t) = \underline{t}(S,t) \cdot \frac{\partial \underline{u}(S,t)}{\partial S}. \tag{10}$$

As implied by its name, this quantity is the convected derivative of the axial stretch ℓ: the identity $d = \dot{\ell}$ is established in Appendix A.1. Note that this Lagrangian measure of the stretching strain differs from the Eulerian strain rate, denoted by d^{E} later, familiar to fluid mechanicians.

A useful identity follows from taking the time derivative of the identity $\underline{T} = \ell \underline{t}$, implied by Eq. (8). This yields $\underline{u}'(S) = \dot{\ell}\underline{t} + \ell\dot{\underline{t}}$. Applying the perpendicular projection operator $\underline{P}_\perp(\underline{t},\cdot)$ on both sides, and using the fact that $\dot{\underline{t}}$ is perpendicular to $\underline{t}$ since $\underline{t}$ is a unit vector at all times, we have

$$\frac{\partial \underline{t}(S,t)}{\partial t} = \frac{1}{\ell(S,t)}\,\underline{P}_\perp\left(\underline{t}(S,t), \frac{\partial \underline{u}(S,t)}{\partial S}\right). \tag{11}$$

This equation will be used to reconstruct the time derivative of the tangent from the centerline velocity $\underline{u}$.

2.3. Incompressibility: radius and related quantities

The radius of the thread in the actual configuration is denoted by $a(S,t)$, the area is $A(S,t)$, and $I(S,t)$ stands for the geometric moment of inertia:

$$A(S,t) = \pi a^2(S,t), \qquad I(S,t) = \frac{\pi a^4(S,t)}{4}. \tag{12}$$

The fluid volume enclosed in an infinitesimal chunk of the thread reads $A(S,t)\,\mathrm{d}s = A(S,t)\ell(S,t)\,\mathrm{d}S$ in the actual configuration, and $A_0(S,t)\,\mathrm{d}S$ in reference configuration, see Fig. 2. As a result, the incompressibility of the fluid is expressed by

$$a(S,t) = \frac{a_0}{\sqrt{\ell(S,t)}}, \qquad A(S,t) = \frac{A_0}{\ell(S,t)}, \qquad I(S,t) = \frac{I_0}{\ell^2(S,t)} \tag{13}$$

where the subscript naught refers to the reference configuration, for which we have $\ell_0 = 1$ by convention: $A_0 = \pi a_0^2$ and $I_0 = \pi a_0^4/4$.

2.4. Material frame, adaptation

To complete the description of the motion, we need to keep track of twist, which gives rise to viscous shear stress. It is defined as the rotation of the cross-sections about the tangent. Let us consider an orthonormal triad, denoted by $(\underline{d}_1(S,t), \underline{d}_2(S,t), \underline{d}_3(S,t))$, which is rigidly attached to the cross-sections. This triad is called the material frame: it follows the motion of the particles inside the viscous thread.

Let us denote $\underline{\omega}(S,t)$ the angular velocity of the material frame, and $\underline{\pi}(S,t)$ the twist-curvature vector. Each one is a Darboux vector, as defined generically in Eq. (1), one being associated with increments of the variable $\sigma = t$ and the other one with increments of $\sigma = S$:

$$\frac{\partial \underline{d}_i(S,t)}{\partial t} = \underline{\omega}(S,t) \times \underline{d}_i(S,t) \tag{14a}$$

$$\frac{\partial \underline{d}_i(S,t)}{\partial S} = \underline{\pi}(S,t) \times \underline{d}_i(S,t), \tag{14b}$$

for any value of the index $1 \leqslant i \leqslant 3$. The vector $\underline{\omega}$ is the angular velocity of the fluid. The twist-curvature vector measures the rate of rotation of the material frame per unit Lagrangian arc length $\mathrm{d}S$: its tangential component measures twist, and its perpendicular components measures curvature.

The fact that the frame $\{\underline{d}_i\}_{1\leqslant i\leqslant 3}$ follows the motion of the fluid particles, and at the same time remains orthonormal at all times, is known as the Kirchhoff kinematic hypothesis. The word 'hypothesis' is used for historical reasons, but it can be justified rigorously by asymptotic analysis. In Ref. [11], for instance, it is shown that the flow inside the thread is shearless in the limit of very thin thread, as in the case of elastic rods [50]. As a consequence of the Kirchhoff hypothesis, the material frame has to stay compatible with the centerline, in the sense that

$$\underline{d}_3(S,t) = \underline{t}(S,t). \tag{15}$$

This kinematic condition couples the rotations of the material frame in the left-hand side with the motion of the centerline in the right-hand side. Note that this condition does not imply inextensibility, as $\underline{t}$ has been defined as a unit vector, even in the presence of stretching ($|\underline{T}| \neq 1$).

The tangential components of the Darboux vectors $\underline{\omega}$ and $\underline{\pi}$ are called the spin velocity $v(S,t)$ and the kinematic twist τ, respectively:

$$v(S,t) = \underline{\omega}(S,t)\cdot\underline{t}(S,t) \tag{16a}$$

$$\tau(S,t) = \underline{\pi}(S,t)\cdot\underline{t}(S,t). \tag{16b}$$

These quantities have appeared under the generic notation Γ_3 in Eq. (3): by this equation, v is given by $v = \dot{\underline{d}}_1\cdot\underline{d}_2$ and $\tau = \underline{d}_1'\cdot\underline{d}_2$. The kinematic twist τ measures the rate of rotation of the material frame about the tangent. Note that it is different from the familiar notion of Frénet–Serret torsion which is irrelevant to the dynamics of threads.

Explicit expressions for the angular velocity and twist-curvature vectors can be found from Eq. (2):

$$\underline{\omega}(S,t) = \underline{t}(S,t)\times\frac{\partial\underline{t}(S,t)}{\partial t} + v(S,t)\,\underline{t}(S,t) \tag{17a}$$

$$\underline{\pi}(S,t) = \underline{K}(S,t) + \tau(S,t)\,\underline{t}(S,t), \tag{17b}$$

where we have introduced the binormal curvature:

$$\underline{K}(S,t) = \underline{t}(S,t)\times\frac{\partial\underline{t}(S,t)}{\partial S} \tag{17c}$$

that depends only on the centerline, and not on the material frame. Consistently with our Lagrangian approach, both the kinematic twist τ and the binormal curvature $\underline{K}$ refer to a unit increment of the Lagrangian coordinate S: they differ from the twist and curvature used in the Eulerian framework, which refer to unit increments of s instead.

2.5. Rates of strain

The strain rates are required in the constitutive laws of the viscous thread. By the identity (A.1) derived in Appendix A, the rate of strain associated with the stretching mode is simply $d(S,t) = \dot{\ell}(S,t)$. The rate of strain associated with the bending and twisting modes is captured by a vector denoted by $\underline{e}$, called strain rate vector and defined as the gradient of angular velocity,

$$\underline{e}(S,t) = \frac{\partial\underline{\omega}(S,t)}{\partial S}. \tag{18}$$

For a rigid-body motion, $\underline{\omega}$ is constant and $\underline{e}$ cancels, as expected.

In Appendix A.2, we show that the axial component of $\underline{e}$ is the time derivative of the kinematic twist τ, and its normal projection is the time derivative of the binormal curvature $\underline{K}$ convected in the material frame. In view of this, we define the rates of strain for the twisting and bending modes as the axial and perpendicular projections of $\underline{e} = \underline{\omega}'$,

$$e_{\mathrm{t}}(S,t) = \underline{\omega}'(S,t)\cdot\underline{t}(S,t) \tag{19a}$$

$$\underline{e}_{\mathrm{b}}(S,t) = \underline{P}_{\perp}\big(\underline{t}(S,t),\underline{\omega}'(S,t)\big). \tag{19b}$$

2.6. A geometrical identity for the rate of twisting strain

The rate of strain for the twisting mode appearing in Eq. (19a) can be rewritten as $e_{\mathrm{t}} = \underline{\omega}'\cdot\underline{t} = (\underline{\omega}\cdot\underline{t})' - \underline{t}'\cdot\underline{\omega} = v' - \underline{t}'\cdot\underline{\omega}$. The derivative of the tangent is given by Eq. (14b) as $\underline{t}' = \underline{\pi}\times\underline{t} = \underline{K}\times\underline{t}$. Permuting the mixed product and using Eq. (14a) to identify the time derivative of the unit tangent, we find

$$e_{\mathrm{t}}(S,t) = \frac{\partial v(S,t)}{\partial S} + \underline{K}(S,t)\cdot\frac{\partial\underline{t}(S,t)}{\partial t}. \tag{20}$$

In a previous work [35] focusing on the case of elastic rods, this equation was used to obtain a natural discretization of twist.

This equation is at the heart of the centerline/spin representation, which uses the centerline position $\underline{x}(S,t)$ and the spin velocity $v(S,t)$ as the primary unknowns. The tangent $\underline{t}$ and binormal curvature $\underline{K}$ appearing in the right-hand side can be reconstructed in terms of the centerline $\underline{x}$. Therefore, Eq. (20) defines the rate of twisting strain in the centerline/spin representation. Note that it couples the twisting degrees of freedom and the centerline degrees of freedom.

Eq. (20) can be seen as an incremental version of the Călugăreanu–White–Füller (CWF) theorem [51–55] which defines the notion of writhing for a closed curve — for a short review on this theorem, see Refs. [56,57]. Its relevance to the dynamics of rods has been discussed by several authors: the CWF theorem has been used in the context of supercoiled DNA [58–61] or polymers [62], and in other contexts such as the dynamics of elastic filaments in a viscous fluid [63,64] or the mechanics of proteins [65]. Here, we use this Eq. (20) as a starting point to derive our discrete viscous thread model.

2.7. Virtual velocities, virtual rates of strain

We need to rewrite the main formulas obtained so far in order to make explicit the dependences (i) on the current configuration, denoted by $\underline{X}_t$, and (ii) on the velocities $\underline{u}$ and v. This shall allow us to introduce *virtual* velocities, denoted by $\hat{\underline{u}}(S)$ and $\hat{v}(S)$. Virtual velocities can be considered as dummy arguments, and are unrelated to the real motion — in particular the equality $\dot{\underline{x}}(S,t) = \hat{\underline{u}}(S)$ does *not* hold. Virtual velocities will make it possible to compute the functional derivatives of the strain rates with respect to the velocities, that are required for the calculation of the viscous forces by the method of Rayleigh.

The current configuration $\underline{X}_t$ is defined by a function of a single variable that maps the arc length S to the centerline position, $\underline{X}_t(S) = \underline{x}(S,t)$. We rewrite Eq. (11) yielding the time derivative of the tangent as $\dot{\underline{t}}(S,t) = \underline{\mathcal{V}}(\underline{X}_t; \underline{u}; S)$ where the operator $\underline{\mathcal{V}}$ is defined in terms of a virtual (generic) velocity by

$$\underline{\mathcal{V}}(\underline{X}; \hat{\underline{u}}; S) = \frac{1}{\ell(S)}\, \underline{P}_\perp\big(\underline{t}(S), \hat{\underline{u}}'(S)\big). \tag{21}$$

In the right-hand side, the axial stretch ℓ and the unit tangent $\underline{t}$ are reconstructed from the current configuration $\underline{X}(S)$ passed as in argument using Eqs. (7) and (8). Similarly, the angular velocity $\underline{\omega}$ is given by Eq. (17a) as $\underline{\omega}(S,t) = \underline{\mathcal{W}}(\underline{X}_t; \underline{u}, v; S)$ where

$$\underline{\mathcal{W}}(\underline{X}; \hat{\underline{u}}, \hat{v}; S) = \hat{v}(S)\, \underline{t}(S) + \underline{t}(S) \times \underline{\mathcal{V}}(\underline{X}; \hat{\underline{u}}; S), \tag{22}$$

the rate of stretching strain is given by Eq. (10) as $d(S,t) = \mathcal{L}_{\mathrm{s}}(\underline{X}_t; \underline{u}; S)$ where

$$\mathcal{L}_{\mathrm{s}}(\underline{X}; \hat{\underline{u}}; S) = \underline{t}(S) \cdot \hat{\underline{u}}'(S), \tag{23}$$

the rate of twisting strain is given by Eq. (20) as $e_{\mathrm{t}}(S,t) = \mathcal{L}^{\mathrm{t}}(\underline{X}_t; \underline{u}, v; S)$ where

$$\mathcal{L}^{\mathrm{t}}(\underline{X}; \hat{\underline{u}}, \hat{v}; S) = \hat{v}'(S) + \underline{K}(S) \cdot \underline{\mathcal{V}}(\underline{X}; \hat{\underline{u}}; S), \tag{24}$$

and the rate of bending strain is given by Eq. (19b) as $\underline{e}_{\mathrm{b}}(S,t) = \underline{\mathcal{L}}^{\mathrm{b}}(\underline{X}_t; \underline{u}, v; s)$ where

$$\underline{\mathcal{L}}^{\mathrm{b}}(\underline{X}; \hat{\underline{u}}, \hat{v}; S) = \underline{P}_\perp\left(\underline{t}(S), \frac{\mathrm{d}\underline{\mathcal{W}}(\underline{X}; \hat{\underline{u}}, \hat{v}; S)}{\mathrm{d}S}\right). \tag{25}$$

As earlier for ℓ and $\underline{t}$, the binormal curvature $\underline{K}$ appearing in Eq. (24) is reconstructed from the current configuration $\underline{X}(S)$ passed in argument, using Eq. (17c). Note that $\mathcal{L}_{\mathrm{s}}$ depends on the linear velocity $\hat{\underline{u}}$ but not on the spin velocity $\hat{v}$. Besides, $\underline{\mathcal{L}}^{\mathrm{b}}$ depends on the derivatives of the virtual velocities through the total derivative of $\underline{\mathcal{W}}$ appearing in its definition; the same holds for $\underline{\mathcal{V}}$ and $\mathcal{L}^{\mathrm{t}}$. All the operators $\underline{\mathcal{V}}$, $\underline{\mathcal{W}}$, $\mathcal{L}_{\mathrm{s}}$, $\mathcal{L}^{\mathrm{t}}$, $\underline{\mathcal{L}}^{\mathrm{b}}$ introduced above depend linearly on the virtual velocities $\hat{\underline{u}}$ and/or $\hat{v}$. The corresponding discrete operators will play a key role in the discrete model.

We have presented the centerline/spin description of the rod, which makes use of the centerline position $\underline{x}(S,t)$ and velocity $\underline{u}(S,t)$, and of the spin velocity $v(S,t)$ as primary unknowns. We are done with the kinematic analysis of the rod, and now proceed to introduce the viscous constitutive laws.

2.8. Dissipation potentials

The viscous constitutive laws can be introduced using the method of Rayleigh potentials [66]. This approach is first illustrated in the simple case of a particle having a single degree of freedom $x(t)$. The viscous drag force reads $f = -\nu\, u$, where ν is the drag coefficient and $u = \dot{x}$ the velocity. This force can be obtained by defining the Rayleigh potential $\mathcal{D}_{\mathrm{p}}(\hat{u}) = \frac{\nu}{2}\, \hat{u}^2$, by deriving it with respect to the virtual velocity, and then by inserting the real velocity:

$$f = -\frac{\partial \mathcal{D}_{\mathrm{p}}(\hat{u})}{\partial \hat{u}}\bigg|_{\hat{u}=u} = -\nu\, u = -\nu\, \dot{x}. \tag{26}$$

Rayleigh potentials provide a natural discretization of the viscous forces for a discrete viscous thread; a similar approach has been followed by Batty and Bridson [67] in the context of 3d fluids with free boundaries.

As illustrated by the example above, the Rayleigh potential expresses the power dissipated by the viscous forces during a virtual motion. For viscous threads, it has three contributions, corresponding to the stretching, twisting and bending modes of deformation:

$$\mathcal{D}(\underline{x};\underline{\hat{u}},\hat{v}) = \mathcal{D}_{\mathrm{s}}(\underline{x};\underline{\hat{u}}) + \mathcal{D}_{\mathrm{t}}(\underline{x};\underline{\hat{u}},\hat{v}) + \mathcal{D}_{\mathrm{b}}(\underline{x};\underline{\hat{u}},\hat{v}). \tag{27}$$

Let us denote the viscous stretching modulus by $D(\ell)$, the viscous twisting modulus by $C(\ell)$ and the viscous bending modulus by $B(\ell)$,

$$D(\ell) = 3\mu A(\ell) = \frac{D_0}{\ell}, \qquad C(\ell) = 2\mu I(\ell) = \frac{C_0}{\ell^2}, \qquad B(\ell) = 3\mu I(\ell) = \frac{B_0}{\ell^2}. \tag{28}$$

The expression of D is due to Trouton [14], and that of C and B can be found in [68,9]. Here, μ is the fluid's dynamic viscosity, $D_0 = 3\mu A_0 = 3\mu(\pi a_0^2)$, $C_0 = 2\mu I_0$ and $B_0 = 3\mu I_0$ are the value of the moduli in reference configuration and A_0 and I_0 are the cross-sectional area and moment of inertia in reference configuration defined in Section 2.3. The dependence of the area A on the stretch ℓ comes from the conservation of volume in Eq. (13).

We propose the following expressions for the Rayleigh potentials:

$$\mathcal{D}_{\mathrm{s}}(\underline{X};\underline{\hat{u}}) = \int_{S_-}^{S^+} \frac{D(\ell(S))}{2\,\ell(S)} \big(\mathcal{L}_{\mathrm{s}}(\underline{X};\underline{\hat{u}};S)\big)^2 \,\mathrm{d}S \tag{29a}$$

$$\mathcal{D}_{\mathrm{t}}(\underline{X};\underline{\hat{u}},\hat{v}) = \int_{S_-}^{S^+} \frac{C(\ell(S))}{2\,\ell(S)} \big(\mathcal{L}^{\mathrm{t}}(\underline{X};\underline{\hat{u}},\hat{v};S)\big)^2 \,\mathrm{d}S \tag{29b}$$

$$\mathcal{D}_{\mathrm{b}}(\underline{X};\underline{\hat{u}},\hat{v}) = \int_{S_-}^{S^+} \frac{B(\ell(S))}{2\,\ell(S)} \big(\underline{\mathcal{L}}^{\mathrm{b}}(\underline{X};\underline{\hat{u}},\hat{v};S)\big)^2 \,\mathrm{d}S. \tag{29c}$$

Here S^- and S^+ denote the Lagrangian coordinates of the endpoints of the thread. Both S^- and S^+ may depend on time even though this time dependence is implicit for the sake of readability. In all the expressions above, ℓ is reconstructed in terms of the first argument $\underline{X}$, as earlier. The stretching contribution $\mathcal{D}_{\mathrm{s}}$ does not depend on the rotational degree of freedom $\hat{v}$ but solely on the centerline velocity $\underline{\hat{u}}$. By the analysis of Section 2.7, $\mathcal{L}_{\mathrm{s}}$, $\mathcal{L}^{\mathrm{t}}$ and $\underline{\mathcal{L}}^{\mathrm{b}}$ represent the rates of strain associated with the three fundamental modes of deformation. Note that they all depend linearly on the virtual velocities, and as a result the Rayleigh potentials $\mathcal{D}_{\mathrm{s}}$, $\mathcal{D}_{\mathrm{b}}$ and $\mathcal{D}_{\mathrm{t}}$ and $\mathcal{D}$ are quadratic forms of their velocity arguments $\underline{\hat{u}}$ and $\hat{v}$; this quadratic dependence reflects the linear character of the viscous constitutive laws.

In Appendix B.1, we show that the expressions of the Rayleigh potential proposed in Eq. (29) correspond (by the method of Rayleigh) to the well-established constitutive laws for thin viscous threads, namely (i) Trouton's law [14] expressing the tension n_{s} in terms of the viscous stretching modulus D and the Eulerian rate of axial strain d^{E},

$$n_{\mathrm{s}} = D d^{\mathrm{E}}$$

and (ii) the expression of the internal moment $\underline{m}$ in terms of the bending modulus B, of the twisting modulus C, and of the Eulerian rate of strain $\underline{e}^{\mathrm{E}}$ of the twisting and bending modes [15]:

$$\underline{m} = \big[C\underline{t}\otimes\underline{t} + B(\underline{\underline{1}} - \underline{t}\otimes\underline{t})\big]\cdot\underline{e}^{\mathrm{E}},$$

where $\underline{\underline{1}}$ denotes the identity matrix.

2.9. Equations of motion

As illustrated by Eq. (26), the viscous force is found by the method of Rayleigh by derivation of the potential with respect to the virtual velocity. Therefore, the resultant of the viscous stress on the centerline is given by

$$\underline{P}_{\mathrm{v}}(S,t) = -\frac{\partial\mathcal{D}(\underline{X}_t;\underline{\hat{u}},\hat{v})}{\partial\underline{\hat{u}}(S)}\bigg|_{(\underline{\hat{u}},\hat{v})=(\underline{u},v)}. \tag{30a}$$

The notation in the right-hand side must be understood as follows: we first take the functional derivative of the potential with respect to its argument $\underline{\hat{u}}$, and later substitute the velocity arguments with their real values, $\underline{\hat{u}} = \underline{u}$ and $\hat{v} = v$. This quantity $\underline{P}_{\mathrm{v}}$ is the resultant of the internal viscous forces, per unit length $\mathrm{d}S$ in reference configuration. It includes the stretching, twisting and bending forces, each contribution being listed in Eq. (27). The force $\underline{P}_{\mathrm{v}}$ depends on the current centerline shape $\underline{X}_t$ and on the real velocities $\underline{u}$ and v, but this dependence is implicit in our notations.

The stress quantity which is dual to the spin velocity v is the net twisting moment arising from the viscous stress. It is given by a similar formula,

$$Q_{\mathrm{v}}(S,t) = -\left.\frac{\partial \mathcal{D}(\underline{X}_t;\hat{\underline{u}},\hat{v})}{\partial \hat{v}(S)}\right|_{(\hat{\underline{u}},\hat{v})=(\underline{u},v)}. \tag{30b}$$

In practice, the functional derivatives in Eqs. (30) are computed by casting the first variation of the Rayleigh potential $\delta\mathcal{D}$ into the form $\delta\mathcal{D} = -\int(\underline{P}_{\mathrm{v}}\cdot\delta\hat{\underline{u}} + Q_{\mathrm{v}}\,\delta\hat{v})\,\mathrm{d}S$. Explicit expressions of $\underline{P}_{\mathrm{v}}$ and Q_{v} are derived in Eq. (B.8) of Appendix B and are shown to be equivalent to those used in the classical Kirchhoff theory of rods.

The equations for the dynamics of the thread are given by the balance of linear and angular momentum:

$$\rho A_0 \ddot{\underline{x}}(S,t) = \underline{P}_{\mathrm{v}}(S,t) + \underline{P}(S,t) \tag{31a}$$

$$\ell J \dot{v}(S,t) = Q_{\mathrm{v}}(S,t) + Q(S,t). \tag{31b}$$

These equations express a balance of momentum, per unit length of the thread $\mathrm{d}S$ in reference configuration. The resultant $\underline{P}_{\mathrm{v}}$ and moment Q_{v} of the viscous forces have been defined in terms of the current positions and velocities by Eqs. (29) and (30). The quantities $\underline{P}(S,t)$ and $Q(S,t)$ are the density of external force and of external twisting moment, respectively, per unit length $\mathrm{d}S$ in reference configuration, including the effect of gravity and surface tension. The coefficient ρ is the volume mass of the fluid, and (ρA_0) and (ℓJ) are the mass of the thread and its moment of inertia about the tangent, respectively; both are again measured per unit reference length $\mathrm{d}S$. Here, J is the moment of inertia per unit length $\mathrm{d}s$ in *actual* configuration, and is given by the usual formula

$$J(\ell) = \int_0^{2\pi}\int_{|r|<a} r^2 \rho r\,\mathrm{d}r\,\mathrm{d}\theta = 2\rho I(\ell), \tag{32}$$

in terms of the geometric moment of inertia I defined in Eq. (13). The presence of a factor ℓ in the left-hand side of Eq. (31b) can be explained by multiplying both sides by $\mathrm{d}S$: this makes appear the moment of inertia $\ell\, J\,\mathrm{d}S = J\,\mathrm{d}s$ of a small segment having length $\mathrm{d}S$ in reference configuration and $\mathrm{d}s$ in actual configuration.

A classical approximation, proposed by Kirchhoff himself, is to neglect the rotational inertia and set

$$J = 0, \tag{33}$$

in the balance of moments (31b). This approximation can be justified by the fact that the kinetic energy associated with rotational inertia scales like $(\ell J)v^2 \sim \ell\rho a^4\,(1/t^*)^2$ for a motion happening on a typical time scale t^*. By contrast the kinetic energy associated with translation of the centerline scales like $\ell\rho A\underline{u}^2 \sim \ell\rho a^2(L/t^*)^2$, where L is the typical length scale of the motion. The energy of the rotational mode is therefore negligible for slender threads, for which $L \gg a$. The consequence is that the rotational inertia is negligible in the thin limit which we consider.

2.10. External loading

The weight of the thread is represented by contributions to $\underline{P}$ and Q that are denoted by $\underline{P}_{\mathrm{g}}$ and Q_{g}:

$$\underline{P}_{\mathrm{g}}(S,t) = \rho A_0 \underline{g}, \qquad Q_{\mathrm{g}}(S,t) = 0, \tag{34}$$

where $\underline{g}$ is the acceleration of gravity.

Forces arising due to surface tension are derived by considering another contribution to $\underline{P}$ and Q, deriving from energy proportional to the area of the lateral boundaries. First, we express the capillary energy based on an approximation of the lateral area:

$$\mathcal{E}_\gamma(\underline{x}) = \int_{S_-}^{S^+} \gamma\, 2\pi a\big(\ell(S)\big)\ell(S)\,\mathrm{d}S, \tag{35}$$

where γ is the surface tension, possibly depending on time and position along centerline, and $2\pi a(\ell)(\ell\,\mathrm{d}S)$ is the lateral area of a cylinder of radius a and length $\mathrm{d}s = \ell\,\mathrm{d}S$. Here, we assume slow variations of the thickness along the centerline, and neglect the small conical angle of the lateral surface.

The capillary force acting on the centerline can be obtained from the first variation $\mathrm{d}\mathcal{E}_\gamma$ of the capillary energy: using the definition of $a(\ell)$ in Eq. (13) and the definition of ℓ in terms of $\underline{x}(S)$ in Eq. (7), we find

$$\mathrm{d}\mathcal{E}_\gamma(\underline{x};\delta\underline{x}) = [\underline{n}_\gamma\,\delta\underline{x}]_{S_-}^{S^+} - \int_{S_-}^{S^+} \underline{P}_\gamma(S)\cdot\delta\underline{x}\,\mathrm{d}S, \tag{36a}$$

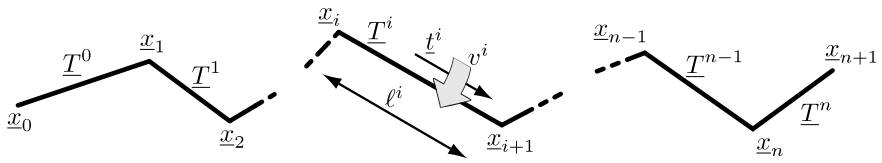

Fig. 3. Discrete setting: centerline is a polygonal curve. Note that we use subscripts for vertex-based quantities, such as vertex positions, and superscripts for segment-based quantities, such as segment length ℓ^i.

where the bracket denotes the boundary term coming from the integration by parts. The coefficients appearing in this variation are identified as a net density of force and twisting moment in the interior ($\underline{P}_\gamma$ and Q_γ) and an internal force ($\underline{n}_\gamma$):

$$\underline{P}_\gamma(S,t) = \frac{\partial \underline{n}_\gamma(S,t)}{\partial S} \tag{36b}$$

$$Q_\gamma(S,t) = 0 \tag{36c}$$

$$\underline{n}_\gamma(S,t) = \gamma\pi a(S,t)\underline{t}(S,t). \tag{36d}$$

These capillary contributions are added to those coming from gravity.

2.11. Summary of the smooth model

In our centerline/spin representation, the *unknowns* are the centerline's position $\underline{x}(S,t)$ and velocity $\underline{u}(S,t)$, and the spinning velocity $v(S,t)$. In terms of these unknowns, the following *kinematic quantities* are calculated successively: the unit tangent $\underline{t}$ and axial stretch ℓ as explained in Section 2.2, the cross-sectional area A and geometrical moment of inertia I as explained in Section 2.3, the binormal curvature $\underline{K}$ as explained in Section 2.4, the linear forms required to compute the rates of strain $\underline{\mathcal{V}}$, $\underline{\mathcal{W}}$, $\mathcal{L}_s$, $\mathcal{L}^t$ and $\mathcal{L}^b$ as explained in Section 2.7. Then, the constitutive equations are obtained by calculating the viscous moduli B, C and D and the dissipation potential $\mathcal{D}$ as explained in Section 2.8, and then the net viscous force $\underline{P}_v$ and twisting moment Q_v by Eq. (30). When inserted into the *equations of motion* (31), this yields the linear acceleration $\dot{\underline{u}}$ and the angular acceleration $\dot{v}$ of the thread.

3. Spatial discretization: discrete viscous threads

In this section, the discrete model of viscous threads is derived in close analogy with the smooth model. Three key ideas are used. First, we extend the centerline/spin representation to discrete space, and parameterize the rotations with a single degree of freedom. Second, we introduce a discrete twist based on the geometrical notion of parallel transport. Third, we derive equations of motion in the discrete setting by variational principles, using discrete Rayleigh potentials.

3.1. Kinematics of centerline

We start by defining discrete quantities such as centerline position, linear and angular velocities and rates of strain. Time discretization will be introduced later in Section 4.

The centerline is discretized using $(n+2)$ vertices, whose positions are denoted by $\underline{x}_0(t)$, $\underline{x}_1(t)$, …, $\underline{x}_{n+1}(t)$, as shown in Fig. 3. In the initial configuration of the thread, the vertices are uniformly spaced; during the simulation new vertices are continuously added from one end and captured from the other end, as explained in Sections 4.3 and 4.4. The vertex positions are collected into a generalized coordinate vector $\underline{X}(t)$, whose size is $3(n+2)$:

$$\underline{X}(t) = \big\{\underline{x}_0(t), \ldots, \underline{x}_{n+1}(t)\big\}. \tag{37}$$

We shall set up a force, assign a mass, and integrate the fundamental law of dynamics at each vertex $\underline{x}_i(t)$. The thin thread behavior is achieved by means of discrete viscous force and twisting moment, which by design converge to $\underline{P}_v(S,t)$ and $Q_v(S,t)$ in the smooth limit.

The segment joining vertices $\underline{x}_i$ and $\underline{x}_{i+1}$ is denoted by

$$\underline{T}^i(t) = \underline{x}_{i+1}(t) - \underline{x}_i(t), \tag{38}$$

as shown in Fig. 3. Following classical conventions, we use subscripts for indices $0 \leqslant i \leqslant n+1$ associated with vertices, and superscripts for indices $0 \leqslant i \leqslant n$ associated with segments. Since the vertex index i plays the role of the Lagrangian coordinate S, the segment vector $\underline{T}^i(t)$ defined above is the discrete equivalent of the material, non-unit tangent $\underline{T}(S,t)$ defined in Eq. (6). More accurately it is, like many other discrete quantities introduced next, an *integrated* quantity: the discrete tangent is approximately the smooth tangent times the discretization length.

The discrete segment length $\ell^i(t)$ and unit tangent $\underline{t}^i(t)$ are defined by formulas similar to Eqs. (7)–(8)

$$\ell^i(t) = \left|\underline{T}^i(t)\right| \tag{39}$$

$$\underline{t}^i(t) = \frac{\underline{T}^i(t)}{\ell^i(t)}. \tag{40}$$

We define the vertex velocities by

$$\underline{u}_i(t) = \frac{\mathrm{d}\underline{x}_i(t)}{\mathrm{d}t}. \tag{41}$$

The rate of strain measuring the stretching of a segment $\underline{T}^i$ reads:

$$d^i(t) = \mathcal{L}^i_s\big(\underline{X}(t); \underline{u}_i(t), \underline{u}_{i+1}(t)\big), \tag{42a}$$

where

$$\mathcal{L}^i_s(\underline{X}; \hat{\underline{u}}_i, \hat{\underline{u}}_{i+1}) = \underline{t}^i \cdot (\hat{\underline{u}}_{i+1} - \hat{\underline{u}}_i). \tag{42b}$$

This definition extends the smooth equation (10) in an obvious way, and warrants $d^i(t) = \dot{\ell}^i(t)$.

The time derivative of the unit tangent is given in terms of the vertex velocities by a geometrical formula analogous to Eq. (11), namely $\dot{\underline{t}}_i(t) = \underline{\mathcal{V}}^i(\underline{X}; \underline{u}_i, \underline{u}_{i+1})$, where the discrete operator $\underline{\mathcal{V}}^i$ attached to segment $\underline{T}^i$ is defined for arbitrary velocities by

$$\underline{\mathcal{V}}^i(\underline{X}; \hat{\underline{u}}_i, \hat{\underline{u}}_{i+1}) = \frac{1}{\ell^i}\underline{P}_\perp\big(\underline{t}^i, \hat{\underline{u}}_{i+1} - \hat{\underline{u}}_i\big). \tag{43}$$

To define the bending strain, we shall later need vertex-based tangents. The latter can be defined in several ways that are all equivalent in the smooth limit, and we opt for one that preserves the unit character of the tangent, namely

$$\tilde{\underline{t}}_i(\underline{x}_{i-1}, \underline{x}_i, \underline{x}_{i+1}) = \frac{\underline{t}^{i-1} + \underline{t}^i}{|\underline{t}^{i-1} + \underline{t}^i|}. \tag{44}$$

The tilde notation is used here and in several other places when we introduce vertex-based versions of quantities that are primarily defined at segments, and *vice-versa*.

Similarly, there are several possible definitions for the discrete binormal curvature vector. A possible definition is:

$$\underline{K}_i(t) = \frac{\underline{t}^{i-1} \times \underline{t}^i}{\frac{1}{2}\,(1 + \underline{t}^{i-1} \cdot \underline{t}^i)}. \tag{45}$$

This particular one emerges in the calculation of the discrete twist, see the forthcoming Eq. (50b). The vector $\underline{K}_i$ is an integrated measure of the smooth binormal curvature vector $\underline{K}(S,t)$ defined in Eq. (17c): the denominator in Eq. (45) converges to 1 in the smooth limit where $\underline{t}^{i-1} \sim \underline{t}^i \sim \underline{t}(S,t)$, while the numerator is equivalent to $\underline{t}^{i-1} \times \underline{t}^i \sim \underline{t}^{i-1} \times (\underline{t}^i - \underline{t}^{i-1}) \sim \underline{K}(S,t)\tilde{\ell}_i$ where $\tilde{\ell}_i$ is the length of the Voronoi cell around vertex $\underline{x}_i$, defined below in Eq. (47).

3.2. Incompressibility: radius and related quantities

Each segment $\underline{T}^i$ carries a volume of fluid V^i and a mass of fluid m^i. Those quantities are initialized based on the prescribed initial segment length, radius and mass density of the fluid. They are conserved during the simulation, except in the case of mesh subdivision, as discussed in Section 4.5. As in the smooth case we use incompressibility to reconstruct the local radius $a^i(t)$ and cross-sectional area $A^i(t)$, assuming a cylindrical segment geometry:

$$A^i(t) = \frac{V^i}{\ell^i(t)}, \qquad a^i(t) = \left(\frac{A^i(t)}{\pi}\right)^{1/2}. \tag{46}$$

The length $\tilde{\ell}_i$ of the Voronoi region near a given vertex is introduced as follows. We leave this length undefined at the end vertices, $i = 0$ and $n+1$. For an interior vertex $\underline{x}_i$ with $1 \leqslant i \leqslant n$, it is the curvilinear distance between the midpoints of the adjacent segments, measured along the polygonal line traced out by the vertices:

$$\tilde{\ell}_i(t) = \frac{\ell^{i-1}(t) + \ell^i(t)}{2} \quad \text{for } 1 \leqslant i \leqslant n. \tag{47}$$

This is a vertex-based discretization length, as opposed to the original segment-based discretization length ℓ^j.

3.3. Material frame, angular velocity

In the discrete case, we decide that the orthonormal triads $(\underline{d}_1^i, \underline{d}_2^i, \underline{d}_3^i)$ live on the segments, like the unit tangent $\underline{t}^i$. This allows the condition of compatibility in Eq. (15) to be easily extended to the discrete case:

$$\underline{d}_3^i(t) = \underline{t}^i(t). \tag{48}$$

Repeating the argument of Section 2.4, one can show that the angular rotation $\underline{\omega}^i$ of the material frame can be decomposed as $\underline{\omega}^i(t) = \underline{\mathcal{W}}^i(\underline{X}; \underline{u}_i, \underline{u}_{i+1}, v^i)$, where the operator $\underline{\mathcal{W}}^i$ for reconstructing material rotation is defined by:

$$\underline{\mathcal{W}}^i\big(\underline{X}; \hat{\underline{u}}_i, \hat{\underline{u}}_{i+1}, \hat{v}^i\big) = \hat{v}^i \underline{t}^i + \underline{t}^i \times \frac{\hat{\underline{u}}_{i+1} - \hat{\underline{u}}_i}{\ell^i}. \tag{49}$$

The quantity $v^i(t)$ is the spin velocity, as depicted in Fig. 3. In our discrete centerline/spin representation, rotations are represented by assigning a degree of freedom v^i to each segment.

3.4. Rate of twisting strain based on parallel transport

In Appendix C.1, we derive a discrete notion of twist τ_i for a polygonal line having an orthonormal frame attached to each segment, that is adapted in the sense of Eq. (48). As in our previous work [35] twist is defined by difference with the geometrical notion of discrete parallel transport along the centerline: the material frames $\underline{d}_j^{i-1}$ and $\underline{d}_j^i$ adjacent to vertex $\underline{x}_i$ are mapped one to another by parallel transport plus a rotation of angle τ_i about the tangent — see Eq. (C.8). This angle τ_i is our discrete notion of twist.

The rate of strain for the twisting mode is defined at the vertices in terms of the twist angle by $e_i^{\mathrm{t}} = \dot{\tau}_i$. This is analogous to the smooth case, see Eq. (A.3a) in Appendix A. The expression of $\dot{\tau}_i$ in our centerline/spin variables is worked out in Eq. (C.14):

$$e_i^{\mathrm{t}} = \mathcal{L}_i^{\mathrm{t}}\big(\underline{X}; \underline{u}_{i-1}, \underline{u}_i, \underline{u}_{i+1}, v^{i-1}, v^i\big), \tag{50a}$$

where the operator for reconstructing the rate of twisting strain is defined by

$$\mathcal{L}_i^{\mathrm{t}}\big(\underline{X}; \hat{\underline{u}}_{i-1}, \hat{\underline{u}}_i, \hat{\underline{u}}_{i+1}, \hat{v}^{i-1}, \hat{v}^i\big) = \hat{v}^i - \hat{v}^{i-1} + \underline{K}_i \cdot \frac{\underline{\mathcal{V}}^{i-1}(\underline{X}; \hat{\underline{u}}_{i-1}, \hat{\underline{u}}_i) + \underline{\mathcal{V}}^i(\underline{X}; \hat{\underline{u}}_i, \hat{\underline{u}}_{i+1})}{2}. \tag{50b}$$

Note the similarity with the smooth rate of strain $e_{\mathrm{t}}(S,t)$ in Eq. (24). The second term in the right-hand side of Eq. (50b) has a geometrical origin. It captures the change of parallel transport resulting from a perturbation to the centerline, an effect that was dubbed holonomy in our previous work. This term is responsible for the coupling of centerline motion with the twisting mode, a phenomenon which appears to be geometrical in essence.

3.5. Rate of change of bending strain

By Eq. (C.13), the rate of strain of the twisting mode e_i^{t} is the tangent projection of the gradient $(\underline{\omega}^i - \underline{\omega}^{i-1})$. In view of the smooth equations (25), we define the rate of strain $\underline{e}_i^{\mathrm{b}}$ of the bending mode as the perpendicular projection of the same vector,

$$\underline{e}_i^{\mathrm{b}} = \underline{\mathcal{L}}_i^{\mathrm{b}}\big(\underline{X}; \underline{u}_{i-1}, \underline{u}_i, \underline{u}_{i+1}, v^{i-1}, v^i\big), \tag{51a}$$

where

$$\underline{\mathcal{L}}_i^{\mathrm{b}}\big(\underline{X}; \hat{\underline{u}}_{i-1}, \hat{\underline{u}}_i, \hat{\underline{u}}_{i+1}, \hat{v}^{i-1}, \hat{v}^i\big) = \underline{P}_\perp\big(\tilde{\underline{t}}_i, \underline{\mathcal{W}}^i\big(\underline{X}; \hat{\underline{u}}_i, \hat{\underline{u}}_{i+1}, \hat{v}^i\big) - \underline{\mathcal{W}}^{i-1}\big(\underline{X}; \hat{\underline{u}}_{i-1}, \hat{\underline{u}}_i, \hat{v}^{i-1}\big)\big). \tag{51b}$$

In the right-hand side above, the operator $\underline{\mathcal{W}}^i$ serves to reconstruct the material rotation $\underline{\omega}^i$: in the case of a real motion, $\underline{e}_i^{\mathrm{b}} = \underline{\mathcal{L}}_i^{\mathrm{b}} = \underline{P}_\perp(\tilde{\underline{t}}_i, \underline{\omega}^i - \underline{\omega}^{i-1})$, which appears to be consistent with the smooth equation (25).

Note that we could multiply the right-hand side of Eq. (51b) by an arbitrary factor $h(\varphi_i)$ converging to $h \to 1$ in the smooth limit $\varphi_i \to 0$. This would define an alternative discrete bending model, equivalent to ours in the smooth limit.

3.6. Generalized velocity

In our centerline/spin representation, the generalized velocity is a vector of dimension $4n+7$, defined by collecting the linear velocities of the vertices, and the angular (spin) velocities of the segments:

$$\underline{U}(t) = \big\{\underline{u}_0(t), v^0(t), \underline{u}_1(t), v^1(t), \ldots, v^n(t), \underline{u}_{n+1}(t)\big\}. \tag{52}$$

This representation is inspired from the centerline/*angle* representation introduced by Langer and Singer in the context of elastic rods [57]. By contrast with these authors, who define the orientation of the cross-section incrementally with respect to the arc length S, we define it incrementally with respect to time t using the spinning velocity v: this makes the matrix governing the dynamics of the thread sparse, as we shall see.

The generalized velocity vector $\underline{U}(t)$ is larger than the generalized coordinate $\underline{X}(t)$ introduced in Eq. (37), as the latter carries no information about frame rotation. Mapping of the indices in $\underline{X}$ and $\underline{U}$ is achieved using a projection operator defined as

$$\underline{\underline{\Pi}}_n = \sum_{i=0}^{n+1} \sum_{j=0}^{2} \underline{\delta}_{3i+j} \otimes \underline{\delta}_{4i+j}. \tag{53}$$

Here $\underline{\underline{\Pi}}_n$ is a matrix of size $(3n+5) \times (4n+7)$, defined with the convention that vector indices start at 0. The index i runs over vertices, the index j over space directions, and $\underline{\delta}_k$ represents the vector whose entries are all 0, except for the k-th entry whose value is 1. The values $k = 3i + j$ and $k = 4i + j$ appearing in subscript are the numbering of the translational degree of freedom for vertex i in direction j in $\underline{X}$, and in $\underline{U}$, respectively. The generalized velocity and positions are then connected by the equation

$$\dot{\underline{X}}(t) = \underline{\underline{\Pi}}_n \cdot \underline{U}(t), \tag{54}$$

which we will use in the implementation to update positions from the velocities.

3.7. Dissipation potentials

As in the smooth case, the Rayleigh potential is defined in terms of a virtual velocity $\hat{\underline{U}} = \{\hat{\underline{u}}_0, \hat{v}^0, \hat{\underline{u}}_1, \hat{v}^1, \ldots, \hat{v}^n, \hat{\underline{u}}_{n+1}\}$, which is not a function of time and is *not* related to real positions through Eq. (54).

The discrete Rayleigh potentials extend the smooth ones defined in Eqs. (29):

$$\mathcal{D}_{\mathrm{s}}(\underline{X}; \hat{\underline{U}}) = \frac{1}{2} \sum_{0 \leqslant i \leqslant n} D^i \big(\mathcal{L}^i_{\mathrm{s}}(\underline{X}; \hat{\underline{u}}_i, \hat{\underline{u}}_{i+1})\big)^2 \tag{55a}$$

$$\mathcal{D}_{\mathrm{t}}(\underline{X}; \hat{\underline{U}}) = \frac{1}{2} \sum_{1 \leqslant i \leqslant n} C_i \big(\mathcal{L}^{\mathrm{t}}_i\big(\underline{X}; \hat{\underline{u}}_{i-1}, \hat{\underline{u}}_i, \hat{\underline{u}}_{i+1}, \hat{v}^{i-1}, \hat{v}^i\big)\big)^2 \tag{55b}$$

$$\mathcal{D}_{\mathrm{b}}(\underline{X}; \hat{\underline{U}}) = \frac{1}{2} \sum_{1 \leqslant i \leqslant n} B_i \big(\underline{\mathcal{L}}^{\mathrm{b}}_i\big(\underline{X}; \hat{\underline{u}}_{i-1}, \hat{\underline{u}}_i, \hat{\underline{u}}_{i+1}, \hat{v}^{i-1}, \hat{v}^i\big)\big)^2. \tag{55c}$$

The stretching contribution involves a sum over all segments, but the sums in the twisting and bending contributions is restricted to *interior* vertices: the strain rates $\mathcal{L}^{\mathrm{t}}_i$ and $\underline{\mathcal{L}}^{\mathrm{b}}_i$ are not defined on the extremal vertices.

The total Rayleigh potential is defined by summing up these contributions:

$$\mathcal{D}(\underline{X}; \hat{\underline{U}}) = \mathcal{D}_{\mathrm{s}}(\underline{X}; \hat{\underline{U}}) + \mathcal{D}_{\mathrm{t}}(\underline{X}; \hat{\underline{U}}) + \mathcal{D}_{\mathrm{b}}(\underline{X}; \hat{\underline{U}}). \tag{56}$$

In Eqs. (55), the discrete moduli are defined by analogy with the smooth moduli in Eqs. (28),

$$D^i = \frac{3\mu^i A^i}{\ell^i}, \qquad C_i = \frac{2\,[\widetilde{\mu I}]_i}{\tilde{\ell}_i}, \qquad B_i = \frac{3\,[\widetilde{\mu I}]_i}{\tilde{\ell}_i}, \tag{57}$$

where μ^i is the fluid's dynamic viscosity which is stored at segments like other fluid properties, A^i is the segment's cross-sectional area reconstructed by Eq. (46), ℓ_i the segment length given by Eq. (39) and $\tilde{\ell}^i$ the length of the Voronoi cell around an interior vertices given by Eq. (47). The factors ℓ_i and $\tilde{\ell}^i$ have been included to warrant convergence to the smooth Rayleigh potentials, which are defined by curvilinear integrals. The factor $[\widetilde{\mu I}]_i$ appearing the twisting and bending moduli is defined at the vertices by linear interpolation over the adjacent segments:

$$[\widetilde{\mu I}]_i = \frac{1}{2} \frac{\mu^{i-1} (A^{i-1})^2 + \mu^i (A^i)^2}{4\pi}. \tag{58}$$

This definition is motivated by the fact that $I = A^2/(4\pi)$ in the smooth case, as shown by Eq. (12). Note that the value of the ratio $B_i/C_i = 3/2$ between the bending and twisting moduli is preserved: in the smooth case, this relation is a consequence of the incompressibility.

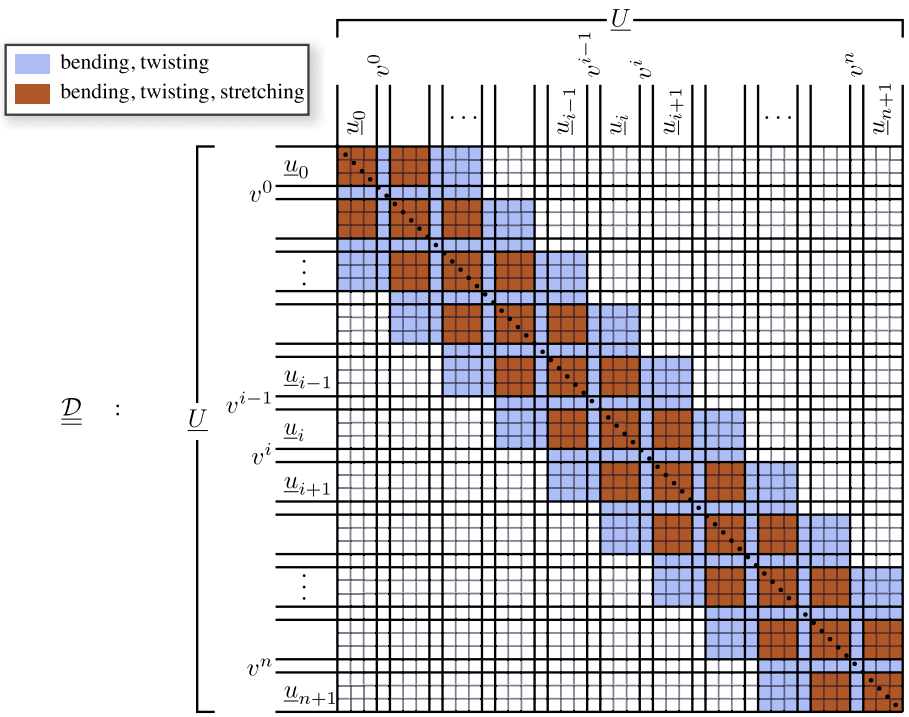

Fig. 4. Band structure of the discrete Rayleigh potential $\underline{\underline{\mathcal{D}}}(\underline{X})$. Colors reveal the contributions coming from the stretching, twisting and bending modes.

3.8. Matrix representation of the Rayleigh potential

One of the main task in each time step is the calculation of the Rayleigh potential $\mathcal{D}(\underline{X}, \underline{\hat{U}})$, whose gradient yields the viscous forces and moments. It is computed symbolically with respect to the argument $\underline{\hat{U}}$, which allows an implicit evaluation of the forces. The potential $\mathcal{D}$ has quadratic dependence on the virtual velocity $\underline{\hat{U}}$, as it represents linear constitutive laws: it is represented by a symmetric matrix $\underline{\underline{\mathcal{D}}}(\underline{X})$:

$$\mathcal{D}(\underline{X}; \underline{\hat{U}}) = \frac{1}{2}\, \underline{\hat{U}} \cdot \underline{\underline{\mathcal{D}}}(\underline{X}) \cdot \underline{\hat{U}}. \tag{59}$$

At each time step, the matrix $\underline{\underline{\mathcal{D}}}(\underline{X})$ is computed as follows, given the configuration of the centerline $\underline{X}$ at the start of the time step. The unit tangents $\underline{t}^i$ are computed using Eqs. (38)–(40). At each vertex $\underline{x}^i$, the rate of strain $\mathcal{L}^i_{\mathrm{s}}$ for the stretching mode, which depends linearly on the symbolic velocity $\underline{\hat{U}}$, is represented as sparse vector, denoted by $\underline{\mathcal{L}}^i_{\mathrm{s}}(\underline{X})$, such that $\mathcal{L}^i_{\mathrm{s}}(\underline{X}; \underline{\hat{U}}) = \underline{\mathcal{L}}^i_{\mathrm{s}}(\underline{X}) \cdot \underline{\hat{U}}$. This sparse vector is built directly from Eq. (42b): it has six non-zero entries, and is filled with the components of the tangent $\underline{t}^i$ at the three slots corresponding to the downstream vertex $\underline{\hat{u}}_{i+1}$, and with minus the components of the same tangent at the three slots corresponding to the upstream vertex $\underline{\hat{u}}_i$. The other linear forms are computed similarly: first, the quantities ℓ^i, $\underline{\tilde{t}}_i$ and $\underline{\underline{K}}_i$ are reconstructed from the current centerline $\underline{X}$ using Eqs. (39), (44) and (45). Next, we successively use Eqs. (43), (49), (50b) and (51b) to compute the sparse tensors $\underline{\mathcal{V}}^i(\underline{X})$, $\underline{\underline{\mathcal{W}}}^i(\underline{X})$, $\underline{\mathcal{L}}^{\mathrm{t}}_i(\underline{X})$ and $\underline{\mathcal{L}}^{\mathrm{b}}_i(\underline{X})$ representing the linear forms $\underline{\mathcal{V}}^i(\underline{X}; \cdot)$, $\underline{\mathcal{W}}^i(\underline{X}; \cdot)$, $\mathcal{L}^{\mathrm{t}}_i(\underline{X}; \cdot)$ and $\underline{\mathcal{L}}^{\mathrm{b}}_i(\underline{X}; \cdot)$, respectively.

To assemble these linear forms into the Rayleigh potential, we first compute the discrete viscous moduli D^i, C_i and B_i in the current configuration $\underline{X}$: we use the incompressibility to reconstruct the area A^i and moment of inertia I^i, as explained in Section 3.2, and then use the definitions of the discrete moduli in Eqs. (57)–(58). The sparse matrix representation of the discrete Rayleigh potential $\underline{\underline{\mathcal{D}}}(\underline{X})$ is then obtained from Eqs. (55) as

$$\begin{aligned}\underline{\underline{\mathcal{D}}}(\underline{X}) = &\sum_{0 \leqslant i \leqslant n} D^i(\underline{X})\, \underline{\mathcal{L}}^i_{\mathrm{s}}(\underline{X}) \otimes \underline{\mathcal{L}}^i_{\mathrm{s}}(\underline{X}) \\ &+ \sum_{1 \leqslant i \leqslant n} \left[C_i(\underline{X}) \underline{\mathcal{L}}^{\mathrm{t}}_i(\underline{X}) \otimes \underline{\mathcal{L}}^{\mathrm{t}}_i(\underline{X}) + B_i(\underline{X}) \big(\underline{\underline{\mathcal{L}}}^{\mathrm{b}}_i(\underline{X})\big)^T \cdot \big(\underline{\underline{\mathcal{L}}}^{\mathrm{b}}_i(\underline{X})\big) \right]\end{aligned} \tag{60}$$

where the successive terms are the stretching, twisting and bending contributions, respectively. Thanks to the ordering conventions for the velocity $\underline{\hat{U}}$, the discrete Rayleigh potential $\underline{\underline{\mathcal{D}}}(\underline{X})$ is a band matrix, as illustrated in Fig. 4.

3.9. Constitutive law

The generalized viscous force $\underline{F}_{\mathrm{v}}$ and the generalized external force $\underline{F}$ collect the force resultants on the vertices $\underline{P}_i$, and the twisting moments Q^i on the segments using the same ordering convention as in the generalized velocity $\underline{U}$:

$$\underline{F}_{\mathrm{v}} = \left(\underline{P}^{\mathrm{v}}_0, Q^0_{\mathrm{v}}, \underline{P}^{\mathrm{v}}_1, \dots Q^n_{\mathrm{v}}, \underline{P}^{\mathrm{v}}_{n+1}\right) \tag{61a}$$

$$\underline{F} = \left(\underline{P}_0, Q^0, \underline{P}_1, \dots Q^n, \underline{P}_{n+1}\right). \tag{61b}$$

Explicit expressions of the external force $\underline{F}$ representing gravity and surface tension are derived in Section 3.11. The discrete viscous force is given by the following constitutive law, by the method of Rayleigh:

$$\underline{F}_{\mathrm{v}}(\underline{X}, \underline{U}) = -\left.\frac{\partial \mathcal{D}(\underline{X}, \hat{\underline{U}})}{\partial \hat{\underline{U}}}\right|_{\hat{\underline{U}}=\underline{U}} = -\underline{\underline{D}}(\underline{X}) \cdot \underline{U}. \tag{62}$$

3.10. Discrete equations of motion

We introduce the generalized mass matrix, which is diagonal, based on the same ordering conventions,

$$\underline{\underline{M}} = \mathrm{diag}\left(\tilde{m}_0 \underline{\underline{1}}, \ell^0 J^0, \tilde{m}_1 \underline{\underline{1}}, \dots, \ell^n J^n, \tilde{m}_{n+1} \underline{\underline{1}}\right), \tag{63a}$$

where $\underline{\underline{1}}$ represents the unit matrix in 3 dimensions. Here, $\tilde{m}_i$ is the vertex-based mass, defined as one half the sum of the mass of the segments adjacent to vertex $\underline{x}_i$:

$$\tilde{m}_i = \sum_{\max(i-1,0) \leqslant j \leqslant \min(i,n)} \frac{m^j}{2}. \tag{63b}$$

For interior vertices, this is the average of the masses of adjacent segments; for terminal vertices, however, there is only one adjacent segment. The vertex mass $\tilde{m}_i$ does not change over time, unless the mesh gets refined. In Eq. (63a), J^i is the moment of inertia of the cylinder attached to segment $\underline{T}^i$ in actual configuration, per unit length, defined by $J^i = 2\rho^i I^i = \frac{m^i}{V^i}\frac{(A^i)^2}{2\pi}$ where $\rho^i = m^i/V^i$ is the mass density of segment i. Our simulation tool has two modes: one in which this complete expression of J^i is used, and another one in which rotational inertia is neglected:

$$J^i = 0. \tag{63c}$$

It follows from the classical scaling argument given at the end of Section 2.9 that rotational inertia has a negligible effect on the motion of a thin thread. We have checked that this is the case in our simulations. All our validation examples shown later have been produced with zero rotational inertia.

The discrete form of the equations of motion (31) writes $\underline{\underline{M}} \cdot \dot{\underline{U}}(t) = \underline{F}_{\mathrm{v}}(\underline{X}(t), \underline{U}(t)) + \underline{F}(t)$: after inserting the constitutive law (62), we have

$$\underline{\underline{M}} \cdot \dot{\underline{U}}(t) = -\underline{\underline{D}}(\underline{X}) \cdot \underline{U} + \underline{F}(t). \tag{64}$$

Recall that the position is updated by $\dot{\underline{X}}(t) = \underline{\underline{\Pi}}_n \cdot \underline{U}(t)$ according to Eq. (54).

3.11. Discrete expressions of external forces: gravity and surface tension

The weight of the thread is taken in account by setting

$$\underline{P}^{\mathrm{g}}_i = \tilde{m}_i \underline{g} \qquad Q^i_{\mathrm{g}} = 0 \tag{65}$$

in the discrete equations of motion. Here $\tilde{m}_i$ is the mass attached to a vertex, defined in Eq. (63b), and $\underline{g}$ the acceleration of gravity.

The discrete surface tension model is based on a capillary energy proportional to the lateral area of the thread,

$$\mathcal{E}_\gamma(\underline{X}) = \sum_{i=0}^{n} \gamma^i \, \Sigma^i(\underline{X}), \tag{66}$$

where γ^i is the fluid's surface tension at segment i. The lateral area Σ^i of segment i is calculated by approximating it as a cylinder, as sketched in Fig. 5. This is much simpler than approximating them as truncated cones, as we did in previous work [41], and yields equivalent results in the limit of a thin thread. The lateral area of the cylinder joining vertices $\underline{x}_i$ and

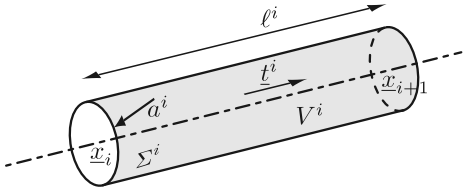

Fig. 5. Discrete surface tension is based on a cylindrical representation of the fluid attached to segments.

$\underline{x}_{i+1}$ reads

$$\Sigma^i = 2\pi a^i \ell^i = 2\sqrt{\pi V^i \ell^i}, \tag{67}$$

after we have used the definition of the volume $V^i = \pi (a^i)^2 \ell^i$. Its gradient reads $\underline{\nabla}_{\underline{x}_i} \Sigma^i = -(\frac{\pi V^i}{\ell^i})^{1/2} \underline{t}^i = -\pi a^i \underline{t}^i$ and $\underline{\nabla}_{\underline{x}_{i+1}} \Sigma^i = +(\frac{\pi V^i}{\ell^i})^{1/2} \underline{t}^i = +\pi a^i \underline{t}^i$. The discrete capillary force at a vertex is given by minus the gradient of the capillary energy (66) with respect to vertex positions,

$$\underline{P}_i^\gamma = \begin{cases} +n^0_{\gamma \mathrm{t}} \underline{t}^0 & \text{if } i = 0 \\ -n^n_{\gamma \mathrm{t}} \underline{t}^n & \text{if } i = n+1 \\ +n^i_{\gamma \mathrm{t}} \underline{t}^i - n^{i-1}_{\gamma \mathrm{t}} \underline{t}^{i-1} & \text{if } 1 \leqslant i \leqslant n \end{cases} \tag{68a}$$

$$Q^i_\gamma = 0, \tag{68b}$$

where we have introduced the capillary tension force

$$n^i_{\gamma \mathrm{t}} = \pi \gamma^i a^i. \tag{68c}$$

This capillary tension is the overpressure in the fluid (γ^i / a^i) caused by the curvature $1/a^i$ of the interface according to the Young–Laplace law, times the cross-sectional area $A^i = \pi (a^i)^2$. The special expressions of the capillary force on the terminal vertices, corresponding $i = 0$ or $i = n+1$ in Eq. (68a), represents the contribution from the cap closing the cylindrical thread at its endpoints — the same effect was captured by the boundary terms in the smooth Eq. (36a). This discrete model for surface tension is validated in Section 5.3.

Contact of the thread with obstacles will be treated using a kinematic method presented in Section 4.3, and not by penalty: there is no need to derive the expressions of the forces of contact.

4. Time discretization, numerical implementation

4.1. Boundary conditions and kinematic constraints

Boundary conditions are enforced by constraining degrees of freedom. We deal with the case of clamped ends, where the velocities $\underline{u}_0$ and $\underline{u}_1$ of the first two vertices and the angular spinning velocity of the first segment v^0 are imposed by the motion of the clamp — a similar condition holds at the other clamped end. Such kinematic constraints are handled by writing the velocity $\underline{U}_{t+\epsilon}$ at the end of the time step as a function of an unconstrained velocity $\underline{Y}$:

$$\underline{U}_{t+\epsilon} = \underline{\underline{B}} \cdot \underline{Y} + \underline{B}', \tag{69}$$

where t is the time at the beginning of the time step, ϵ is the time step duration, and $\underline{Y}$ collects the velocities of the unconstrained degrees of freedom. This vector $\underline{Y}$, whose size r may change over time as kinematic constraints are created or destroyed, is the main unknown of the time step.

The matrix $\underline{\underline{B}}$ and the vector $\underline{B}'$ in Eq. (69) are constructed as follows. Let b be the strictly increasing numbering of the unconstrained degrees of freedom, $b(0) < b(1) < \cdots < b(r-1)$, active at the end of the time step. The matrix $\underline{\underline{B}}$ dispatches the unconstrained degrees of freedom stored in $\underline{Y}$ into the original velocity vector $\underline{U}_{t+\epsilon}$. It is sparse, of size $(4n+7) \times r$, and is filled with ones at entries $B_{b(i),i} = 1$ for $0 \leqslant i \leqslant r-1$, and with zeros elsewhere. The vector $\underline{B}'$ is filled with the known velocities of the constrained degrees of freedom, by fetching the motion of rigid bodies that fix the motion of the clamped ends. The other entries of $\underline{B}'$ correspond to unconstrained degrees of freedom and are set to zero by convention. As a result we have $\underline{\underline{B}}^T \cdot \underline{B}' = \underline{0}$.

As an illustration, the case of no active kinematic constraint is handled by setting $r = 4n+7$, $b(i) = i$, $\underline{B}' = 0$, and $\underline{\underline{B}} = \underline{\underline{1}}$ is the square identity matrix. The case of a viscous thread clamped at both ends with imposed translational velocities $\underline{u}^1_{\text{clamp}}$ and $\underline{u}^2_{\text{clamp}}$, and twisting angular velocities v^1_{clamp} and v^2_{clamp} is handled by

Require: $\underline{x}_i(t)$, $\underline{u}_i(t)$, $v^i(t)$ {initial positions and velocities}
Require: ϵ {time step}
Require: m^i, V^i, μ^i, γ^i {fluid properties}
Require: $\underline{\underline{B}}$ and $\underline{\underline{B}}'$ {boundary conditions}
1: assemble $\underline{X}_t$ and $\underline{U}_t$ {Eqs. (37) and (52)}
2: compute $\underline{\underline{\mathcal{D}}}(\underline{X}_t)$ {Rayleigh potential, Section 3.8}
3: compute $\underline{\underline{M}}$ {Eqs. (63)}
4: compute $\underline{F}(t)$ {external force, Section 3.11 and Eq. (61b)}
5: solve for $\underline{Y}$ {Eq. (73)}
6: reconstruct $\underline{U}_{t+\epsilon}$ {Eq. (69)}
7: update $\underline{u}_i(t+\epsilon)$, $v^i(t+\epsilon)$ {Eq. (52)}
8: update $\underline{x}_i(t+\epsilon)$ {Eq. (74)}

Algorithm 1: The dynamical sequence: this part of the time step is concerned with updating positions and velocities by integrating the equations of motion.

$$r = 4n + 7 - 2\times 7 = 4n - 7 \tag{70a}$$

$$b(i) = i - 7 \tag{70b}$$

$$\underline{B}' = \left(\underline{u}^1_{\text{clamp}}, v^1_{\text{clamp}}, \underline{u}^1_{\text{clamp}}, 0, \underline{0}, \ldots, \underline{0}, 0, \underline{u}^2_{\text{clamp}}, v^2_{\text{clamp}}, \underline{u}^2_{\text{clamp}}\right). \tag{70c}$$

In the presence of kinematic constraints, the equations of motion need to be projected onto the set of unconstrained degrees of freedom. This is achieved by left-multiplying both sides of Eq. (64) by $\underline{\underline{B}}^T$:

$$\underline{\underline{B}}^T \cdot \underline{\underline{M}} \cdot \dot{\underline{U}}(t) = \underline{\underline{B}}^T \cdot \left(-\underline{\underline{\mathcal{D}}}\left(\underline{X}(t)\right) \cdot \underline{U}(t) + \underline{F}(t)\right). \tag{71}$$

4.2. Time-stepping: dynamical sequence

At each time step, the updated position $\underline{X}_{t+\epsilon}$ and velocity $\underline{U}_{t+\epsilon}$ must be determined from the actual position $\underline{X}_t$ and velocity $\underline{U}_t$. We discretize Eq. (71) in time as follows: the viscous force $(-\underline{\underline{\mathcal{D}}} \cdot \underline{U})$ is evaluated implicitly with respect to velocity but explicitly with respect to position, while the other forces $\underline{F}$ are evaluated explicitly,

$$\underline{\underline{B}}^T \cdot \underline{\underline{M}} \cdot \frac{\underline{U}_{t+\epsilon} - \underline{U}_t}{\epsilon} = \underline{\underline{B}}^T \cdot \left(-\underline{\underline{\mathcal{D}}}(\underline{X}_t) \cdot \underline{U}_{t+\epsilon} + \underline{F}(t)\right). \tag{72}$$

In this sense, the scheme is semi-implicit. This choice combines excellent robustness, as demonstrated later on by the validation examples, and ease of implementation.

The final form of our dynamic update rule is obtained by inserting the unconstrained velocities $\underline{Y}$ defined by Eq. (69) into equation above:

$$\left[\underline{\underline{B}}^T \cdot \left(\underline{\underline{M}} + \epsilon\underline{\underline{\mathcal{D}}}(\underline{X}_t)\right) \cdot \underline{\underline{B}}\right] \cdot \underline{Y} = \underline{\underline{B}}^T \cdot \left(\epsilon\left(-\underline{\underline{\mathcal{D}}}(\underline{X}_t) \cdot \underline{\underline{B}}' + \underline{F}(t)\right) - \underline{\underline{M}} \cdot \left(\underline{\underline{B}}' - \underline{U}_t\right)\right). \tag{73}$$

This dynamic update is a linear equation for the unknown velocity Y: it requires only a linear solve. The matrix inside the square brackets in the left-hand side is symmetric, positive definite for any value of the time increment $\epsilon > 0$, and has the same band structure as $\underline{\underline{\mathcal{D}}}$, see Fig. 4. As a result, the linear problem for $\underline{Y}$ can be solved using efficient and robust solvers. In Eq. (73), we recall that $\underline{\underline{B}}$ and $\underline{\underline{B}}'$ encode kinematic constraints, $\underline{\underline{M}}$ is the mass matrix, $\underline{\underline{\mathcal{D}}}$ the Rayleigh potential capturing viscous stress, $\underline{F}(t)$ the external loading and $\underline{U}_t$ the velocity at the start of the time step.

The external force $\underline{F}(t)$, which includes in particular the effect of capillary forces, has been treated explicitly. We have tested an implicit treatment of surface tension but have not observed any significant improvement on the robustness of the simulation: the explicit treatment of surface tension is not the most limiting factor.

Once the linear equation for $\underline{Y}$ has been solved, the generalized velocity $\underline{U}_{t+\epsilon}$ is reconstructed by means of Eq. (69). Positions are then incremented using a discrete version of Eq. (54),

$$\underline{X}_{t+\epsilon} = \underline{X}_t + \epsilon\underline{\underline{\Pi}}_n \cdot \underline{U}_{t+\epsilon}. \tag{74}$$

We call *dynamical sequence* the part of the time step concerned with integrating the equations of motion in time. This involves constructing and solving Eq. (73), and yields the update of velocities $\underline{U}_{t+\epsilon}$, and of positions $\underline{X}_{t+\epsilon}$ by Eq. (74). The dynamical sequence is summarized in Algorithm 1. The other part of the time step, detailed in the following sections, takes care of the interactions of the thread with its environment, including collisions and creation of vertices to represent inflow boundary conditions.

4.3. Fluid container

We consider viscous threads obtained by continuously extruding fluid from a container: in the present section, we explain how this inflow boundary condition is implemented. In the experiments, it is achieved by a syringe actuated by a

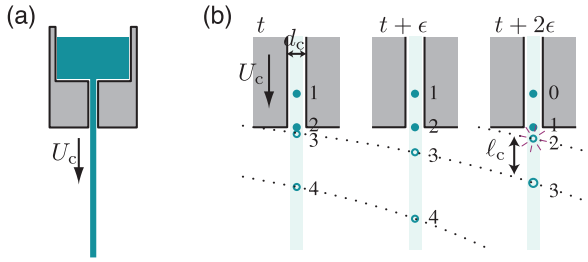

Fig. 6. The thread is formed by extruding fluid from a container at a prescribed velocity. (a) Physical model. (b) Numerical model. Clamped boundary conditions are enforced by prescribing the position and velocities of the two top-most vertices (filled disks), and blocking the rotation of the first segment joining them. Open circles denote unconstrained vertices and dashed curves are the timelines of the vertices. The first two vertices are kept at a fixed position with respect to the container, and mass is continuously added into the second segment. A new vertex is periodically created from top (vertex labeled '2' appearing at time $t+2\epsilon$).

step motor, controlling the volume rate Q_c of the fluid. Let d_c be the diameter of the container, as depicted in Fig. 6a, and $A_c = \pi \frac{{d_c}^2}{4}$ be the area of the opening. The imposed volume rate sets an ejection velocity $U_c = Q_c/A_c$ of the thread relative to the container.

We found that a good discretization of the container is crucial to warrant convergence and reproducibility of the overall behavior of the thread. The discretization proposed here captures the subtle patterns produced by the viscous sewing machine at large fall heights [42]. We tried simpler implementations of the container, but found that they induce spurious oscillations of the thread and failed at reproducing the correct sewing machine patterns.

Our discrete container model is sketched in Fig. 6b. At all times, two vertices are located inside the container, as denoted by the filled disks in the figure. At the beginning of each dynamic step, their velocity is constrained to the value $\underline{u}^1_{\text{clamp}} = (\dot{z}_c(t) - U_c)\,\underline{e}_z$, where $z_c(t)$ is the prescribed height of the container as a function of time and $\underline{e}_z$ is the vertical unit vector pointing upwards. The rotation of the segment joining these first two vertices is blocked, $v^1_{\text{clamp}} = 0$. These clamping conditions are enforced by the method of Section 4.1, see Eq. (70).

After the dynamic step, the position of the two top-most vertices is systematically reset, so as to make the second vertex coincide with the opening of the container, and to make the first vertex lie at a distance ℓ_c above it, where ℓ_c is the parameter determining the mesh size. At each time step, the extrusion of the fluid by the container is captured by increasing the volume of fluid of the *second* top-most segment by $(\epsilon\, Q_c)$ and, correspondingly, its mass by $(\rho\, \epsilon\, Q_c)$, where ϵ is the time step. Whenever the volume of this second segment exceeds the value $(A_c\, \ell_c)$, this segment is split, and a new vertex is inserted between the second and third vertices; the fluid material in ecess is then assigned to the new segment, as sketched in Fig. 6b. As a result, new segments are periodically emitted just below the container, *with an initial length set by the discretization parameter* ℓ_c. Even though all segments were created equal, their length is inhomogeneous along the thread as a result of the stretching by gravity, and of the optional adaptive mesh subdivision which is discussed later.

4.4. Collisions on a hard surface

Falling under its own weight, the thread generally ends up hitting a surface, which can be at rest (as in the steady coiling geometry of Section 5) or in motion (as in the sewing machine experiment of Section 6.2). We explain here how this free boundary is handled. The thread is assumed to stick perfectly to the surface, and gets carried away by it when it is in motion. This motion is prescribed before the start of the simulation: two-way coupling of the thread and the obstacles is not considered.

Detection of collisions with the surface is done by comparing the distance of vertices to the surface, to the radius a^i of the adjacent segments defined in Eq. (46). In all the examples shown, the surface is flat.

Two methods can be used to respond to collisions. The user must pick one at the start of the simulation through a parameter c. The simple 'capture and continue' mode ($c = \texttt{cc}$) is sufficient in the simple geometry of steady coiling, but we found that the more accurate 'time roll-back' ($c = \texttt{rb}$) mode is required in order to correctly predict the complex sewing machine patterns on a moving surface.

4.4.1. 'Capture and continue' mode

In the 'capture and continue' mode ($c = \texttt{cc}$), we walk along the thread in the descending direction, starting from the nozzle, and check for collisions with the ground. In the case where new collisions are detected, the colliding vertex nearest to the nozzle is found, and the thread is cut at the next vertex: all the vertices beyond the cut point are removed from the simulation at subsequent times, and are passively advected by the floor. The two terminal vertices that are retained are subjected to a clamped boundary condition, see Eq. (70): $\underline{u}^2_{\text{clamp}}$ is set by the motion of the floor and the rotation is blocked, $v^2_{\text{clamp}} = 0$.

We found that this simple response method correctly predicts simple deposition patterns, but induces large, spurious fluctuations of the acceleration in some circumstances. These oscillations are caused by the delay in transferring the vertical momentum following a collision: this transfer occurs during the time step following the collision, when the position

constraints start to take effect. With this method, the thread penetrates into the obstacle by a small irregular depth, proportional to the time step duration, which amounts to assign an unphysical rugosity to the surface.

4.4.2. 'Time roll-back' mode

The oscillations were removed by using time *roll-back*, a technique which allows for a more accurate handling of collisions. When roll-back is used ($c = \texttt{rb}$), we check for collisions after every time step: whenever a new collision occurs, the time is rolled back to the start of the time step and the time step is discarded. A new, shorter time step is attempted. Its duration is such that it ends at the collision time estimated from the previous iteration: roll-back is always used in combination with time adaptation. In addition, the motion of the colliding vertices are constrained in the new time step, in such a way that they come in contact with the obstacle at the end of the time step. Roll-back can be viewed as an iterative predictor–corrector or iterative constraint refinement method [69]. A new unexpected collision may indeed take place during the second tentative time step, in which case a third attempt is done, etc. A list of expected collisions is kept and updated each time a time step is discarded.

Roll-back removes the two main limitations of the straightforward 'capture and continue' implementation: it suppress the delay in transferring momentum from the obstacle to the thread, and makes the thread land exactly at the surface of the obstacle, thereby removing the unwanted rugosity. We found that roll-back suppresses the spurious oscillations in acceleration very effectively.

4.5. Optional adaptive mesh subdivision

In the experiments of Morris [13], which we reproduce in Section 6.2, gravity stretches the thread by a factor which can be as large as 10 to 100. In the absence of mesh refinement, the segments in the bottom part of the thread would be considerably longer than those at the top. A good spatial resolution is needed at the bottom in order to resolve the coil having a small radius. To achieve optimal performance, we have implemented mesh refinement by subdivision. This mesh refinement is optional, and is only used in the sewing machine example of Section 6.2.

Mesh subdivision is implemented as follows. The user specifies a refinement criterion through a function $f(\ell, \ell_0, z)$ having boolean values, which depends on the current length ℓ of a segment, on its initial length ℓ_0 and on its current elevation z — an example is provided in Eq. (77). At the end of every dynamic step detailed in Algorithm 1, the segments such that f is true are marked as needing subdivision; in a second pass, those segments are actually subdivided. This subdivision is carried out by inserting a new vertex, and splitting the segment. The position $\underline{x}_i$ and velocity $\underline{u}_i$ of the new vertex are calculated by an interpolation of order 4 based on the positions and velocities of its neighboring vertices. These neighboring vertices are always considered in their state before the subdivision has started: in the case of concurrent subdivision of adjacent segments, this warrants that the result is independent of the order in which the marked segments are processed. The mass m^j stored in the original segment is equally split among the two subsegments. The viscosity μ^j, surface tension γ^j, spinning velocity v^j of the new subsegments are all computed by an interpolation of order 2 based on the values of the former segment and of its neighbors. Finally, the volume V^j of the subsegments is computed by first considering an interpolation of the cross-sectional area A^i at order 4, which is then multiplied by the length of the subsegment. This procedure and the interpolation orders have been chosen in such a way that the viscous twisting and bending forces, which depend on the derivatives of order up to four of the positions, remain smooth upon subdivision.

4.6. Summary of a time step

The full time step is recapitulated in Algorithm 2. To avoid dealing with the initial impact of the thread onto the obstacle, the initial configuration of the thread is clamped into the floor, and we use the clamp-clamp boundary conditions of Eq. (70c) at all times in all the examples; the influence of this initial configuration is limited to a short transient period.

5. Validation in a steady coiling geometry

We proceed to validate our discrete model, verify our implementation, and check convergence in the smooth limit. We consider the steady coiling motion of a viscous thread stretched by gravity and impinging on a surface at rest, as shown in Fig. 7b. Our simulation results are compared to reference solutions kindly provided by N. Ribe, which are based on numerical continuation of the time-independent problem expressed in the co-rotating frame [9], and solved using the AUTO-07 software [70].

5.1. Validation of bending, stretching, gravity, inertia and collisions

The following set of parameters are used for validation and verification: the fluid's dynamical viscosity $\mu = 0.2$ and mass density $\rho = 5 \times 10^{-4}$, the acceleration of gravity $g = 9.81$, the area $A_c = 6.44 \times 10^{-3}$ of the circular outlet of the container and the fluid's volume rate $Q_c = 3.96 \times 10^{-3}$. The surface tension γ is set to zero until we validate surface tension in Section 5.3. The floor is at rest.

Require: $\underline{x}_i(t)$, $\underline{u}_i(t)$, $v^i(t)$ {initial positions and velocities}
Require: ϵ {time step}
Require: m^i, V^i, μ^i, γ^i {fluid properties}
Require: A_c, Q_c, ℓ_c {container properties}
Require: c {collision mode}
Require: f {subdivision criterion}
1: compute $\underline{\underline{B}}$ and $\underline{B}'$ {clamp-clamp boundary conditions, Eq. (70)}
2: do dynamical sequence {Algorithm 1}
3: enforce inflow boundary condition {container, Section 4.3}
4: treat collisions with the floor {depends on c, Section 4.4}
5: optionally, refine by subdivision {based on criterion f, Section 4.5}
6: update floor position {motion of the moving belt is prescribed}

Algorithm 2: Outline of a time step, which includes the dynamic sequence, the interaction with the container and the floor, and the optional mesh subdivision. Note that in the time roll-back mode ($c = \texttt{rb}$), this algorithm may abort at step 4 if new collisions occur, as explained in Section 4.4.2: in that case, the time step is discarded, and a new one is attempted using a smaller value of ϵ.

Three dimensionless groups characterize the properties of the fluid and the container [11]:

$$\Pi_1 = \left(\frac{\nu^5}{g\,{Q_c}^3}\right)^{1/5}, \qquad \Pi_2 = \left(\frac{\nu\,Q_c}{g\,{d_c}^4}\right)^{1/4}, \qquad \Pi_3 = \frac{{d_c}^2\gamma}{Q_c\mu}, \tag{75}$$

where $\nu = \mu/\rho$ is the kinematic viscosity; the diameter of the container's circular opening d_c and the extrusion velocity $U_c = Q_c/A_c$ have been defined in Section 4.3. The numerical values of the dimensionless groups are $\Pi_1 = 7000$, $\Pi_2 = 7$ and $\Pi_3 = 0$ for the set of parameters listed above. This corresponds to significant stretching: the radius decreases by a factor of order 2 during the course of the descent for the range of heights considered below.

Based on the acceleration of gravity g and on the kinematic viscosity ν, one can define a natural length scale L^* and a natural time scale T^* by

$$L^* = \left(\frac{\nu^2}{g}\right)^{1/3}, \qquad T^* = \left(\frac{\nu}{g^2}\right)^{1/3}. \tag{76}$$

Using the above numerical values, $L^* = 25.36$ and $T^* = 1.61$; these scales are used to make the simulation results dimensionless when comparing to the reference solution.

Two additional discretization parameters are needed in the simulation: the initial segment length ℓ_c, introduced in Section 4.3, and the time step ϵ. We take $\ell_c = 0.025$ and $\epsilon = 0.02$. Note that the average number of particles emitted per time step is $(\epsilon\,U_c/\ell_c) = 0.49$: a good trade-off between accuracy and efficiency requires that this number is of order 1. Collisions with the floor are treated using the simple 'capture and continue' method ($c = \texttt{cc}$). Mesh refinement is disabled (f always evaluates to 'false').

N. Ribe provided his reference solution [9] to us in the form of data for the coiling radius or the coiling frequency, as a function of the fall height. To produce simulation data which can be compared to this reference solution, a range of fall heights $H(t)$ is swept in a single simulation run. The motion of the container is prescribed in a sequence of up to three phases. At initial time $t = 0$, it is placed at height H_0. It is left still until time $t = t_1$, when the steady coiling is established. Then, the container is moved upwards at a prescribed velocity $\dot{z}_c = V_c$ that is much smaller than the extrusion velocity U_c, until time $t = t_2$. In a last phase, from time $t = t_2$ to the end of the simulation, $t = t_f$, the container is moved slowly downwards at a velocity $\dot{z}_c = -V_c$. We use $t_1 = 30$, $t_2 = 1530$, $t_f = 3030$ and $V_c = 0.02$, which is 30 times slower than the extrusion velocity U_c, and $H_0 = 1.25$.

Validation results are shown in Fig. 7. Most of the time, the simulation lays down a thin curve (brown and blue) in the plane (H, R), where $R = (x^2 + y^2)^{1/2}$ is the distance of the point of contact of the thread with the floor, to the axis passing through the nozzle. This indicates a steady coiling regime. When the container is moved up (brown curve), the simulated radius R follows closely the reference solution, until the latter folds back onto itself. The portion of the reference curve immediately past the fold point is known to be unstable [11]. The simulation then goes to a transient regime, labeled 'C' in Fig. 7a and shown in Fig. 10. It then settles to a different coiling mode having a smaller radius. A series of such bifurcations is observed in the simulation, a behavior that has been observed in experiments too [11]. A similar sequence of transitions is observed when the container is moved down. As multiple coiling solutions are in competition, a hysteretic behavior is observed: the transition from the second largest coiling radius to the largest one occurs at a fall height 'D' when the container is moved downwards, which is smaller than the fall height 'C' corresponding to the opposite transition (when the container was moved upwards): see Figs. 7 and 10.

In addition, we observe the occurrence of a folding mode in the interval $0.72 > H/L^* > 0.47$ when the container moves down; the competition between the coiling and folding modes is discussed in Ref. [71]. The small gap between the blue and brown curves in the left part of Fig. 7a can be attributed to the fact that the velocity of the container $\dot{z}_c = \pm V_c$ is small but finite. Overall, the simulation is in very good agreement with the reference curve, and reproduces the details of its meandering shape. This validates the various physical ingredients of the model, namely viscous bending and stretching, gravity, inertia and contact with the floor.

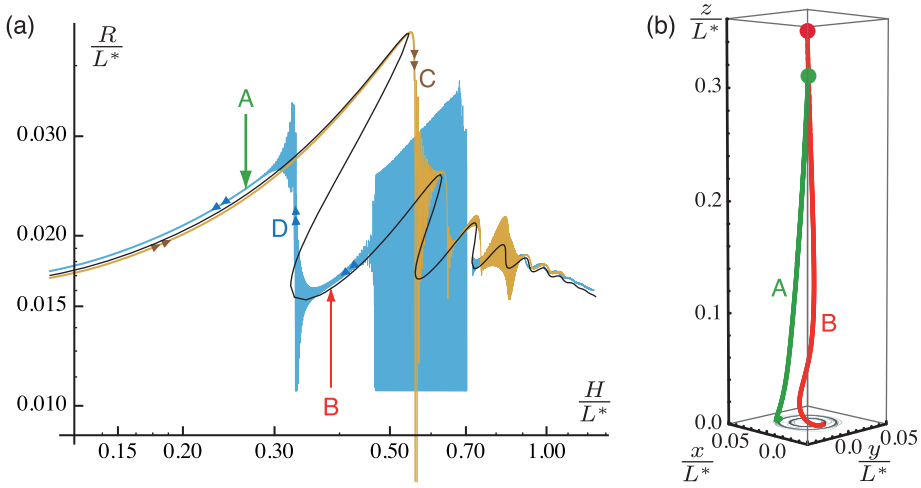

Fig. 7. Validation in a steady coiling geometry, with $\Pi_1 = 7000$, $\Pi_2 = 7$ and $\Pi_3 = 0$ (no surface tension). (a) The coiling radius $R = (x^2 + y^2)^{1/2}$ is recorded continuously as the fall height H is varied, by slowly moving the container upwards (brown curve) and then downwards (blue curve). It is compared against the reference solution of N. Ribe obtained by numerical continuation (black), after rescaling by the length scale L^*. Note the abrupt changes in the coiling radius at places where the reference solution folds back onto itself, as expected. Filled regions correspond to a rapidly varying radius, either because the thread goes to a steady folding mode, as happens around $H = 0.60$, or because of a transient regime following a branch jump. (b) Two typical configurations of the thread, for different fall heights. Note that the fundamental mode of a hanging viscous string is excited in 'A', while its first harmonic is excited in 'B': the red curve has a node near $z/L^* = 0.05$. (For interpretation of the references to color in this figure caption, the reader is referred to the web version of this article.)

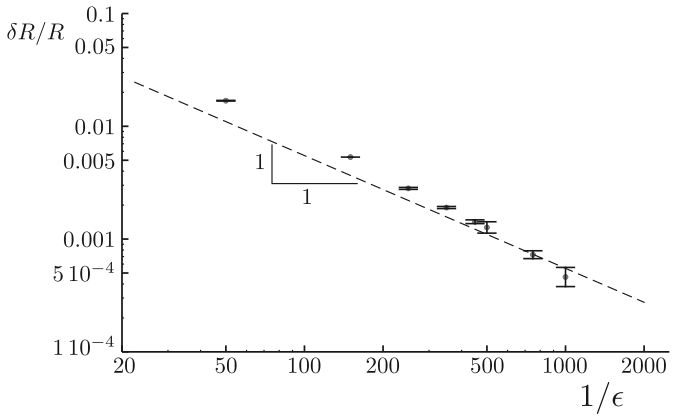

Fig. 8. Convergence towards the reference solution in steady coiling geometry, showing the relative error on the coiling radius $\delta R/R$ as a function of the discretization parameters. Note that the mesh size ℓ_c is decreased along with the time step ϵ: we use $\ell_c = 1.25\epsilon$ in all simulation runs. The same set of physical parameters are used as in Fig. 7, except for the fall height $H = 1.01$ which is constant.

A detailed run such as the one shown in Fig. 7, corresponding to a total simulation time $t_f = 3030$ and a total number of time steps $t_f/\epsilon \approx 150 \times 10^3$, runs in about 30 min on a 2.6 GHz Intel Core i7 processor using 8 GB of memory. The maximum number of vertices, when the fall height is maximum, is 460, corresponding to approximately 1800 degrees of freedom.

5.2. Analysis of convergence

Convergence of the solution towards the reference solution of N. Ribe [9] is shown in Fig. 8 as a function of the discretization parameters. We use the same set of physical parameters as in Section 5.1, except for the fall height which is fixed to $H = 1.01$ and remains constant in time, $\dot{z}_c = 0$.

Convergence is challenging in the presence of collisions on the floor, and we found it necessary to use the time roll-back mode ($c = \texttt{rb}$) to obtain good convergence. Mesh subdivision is switched off, as in the previous section (f is always set to false). Each data point in the convergence plot in Fig. 8 was obtained by running a simulation using a specific pair of values (ϵ, ℓ_c) of the time step and discretization length. Both were varied together, keeping their ratio constant: $\ell_c = 1.25\epsilon$. In each simulation run, the coiling radius R is measured in our simulation after the initial transient period, and then averaged over several periods. It is then compared to the reference value provided by N. Ribe.

The convergence of our numerical method is confirmed by the fact that the residual error goes to zero. The convergence appears to be linear in the discretization parameters.

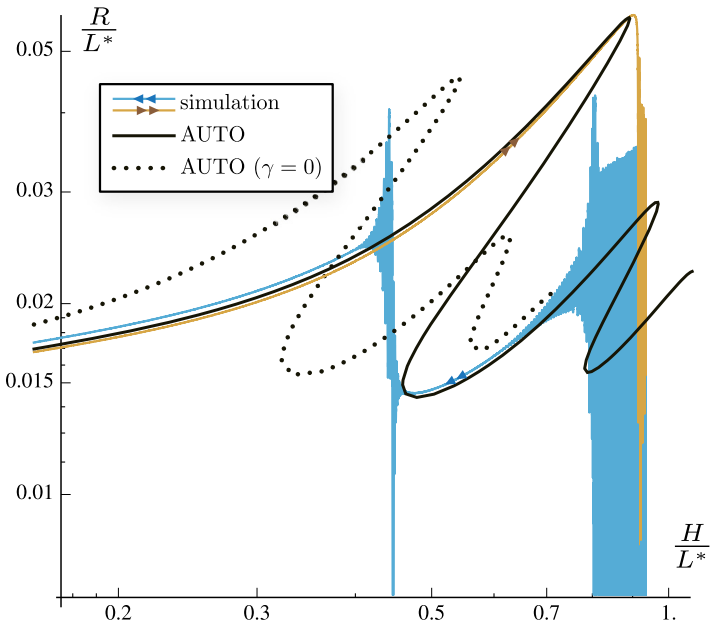

Fig. 9. Validation of surface tension using steady coiling ($\Pi_1 = 7000$, $\Pi_2 = 7$, $\Pi_3 = 10.3 \times 10^{-3}$). The same parameters are used as in Fig. 7, except for the non-zero surface tension $\gamma = 10^{-3}$. A good agreement is obtained with the reference curve that takes surface tension into account (solid black curve). The reference solution with zero surface tension is shown for comparison (dotted line).

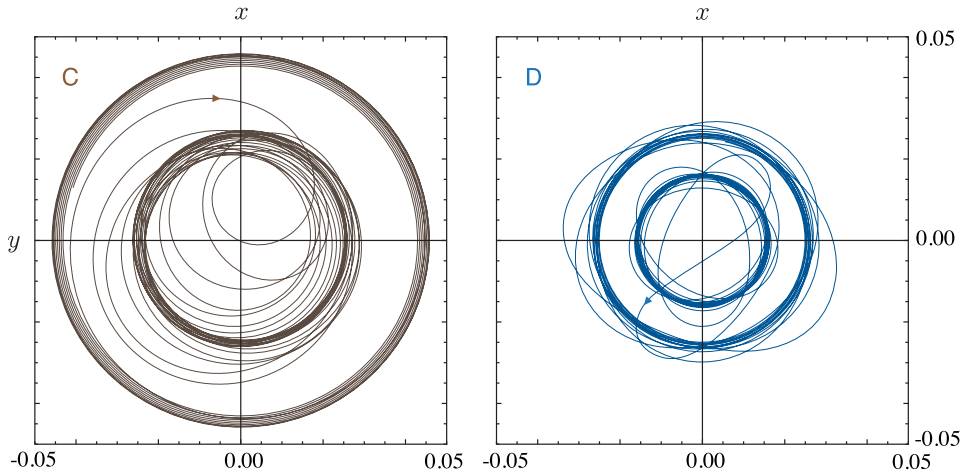

Fig. 10. Trace laid out by the thread in the simulation, in the transient regimes following the jumps labeled 'C' and 'D' in Fig. 7. In 'C', the fall height is slowly increased and the thread jumps to a solution having a smaller radius; in 'D', the fall height is slowly decreased, and the thread jumps to a solution having a larger radius. Same simulation parameters as in Fig. 7.

5.3. Validation of surface tension

With the aim to validate our discrete model for surface tension, we repeat the validation shown in Fig. 7 using the same set of physical and numerical parameters, except for the surface tension coefficient, now set to $\gamma = 10^{-3}$. The corresponding dimensionless parameter is $\Pi_3 = 10.3 \times 10^{-3}$. Surface tension has a marked effect on the coiling radius, as shown by comparison of the solid and dashed black curves in Fig. 9. We obtain a good agreement between the simulation and the new reference curve. This validates our discrete surface tension model.

6. Discussion

6.1. Transient regimes

Even though the steady coiling geometry provides a convenient set-up for validation and verification, our numerical method can solve the non-steady dynamics of viscous threads. As an illustration, transient regimes following jumps from one branch of steady coiling solutions to the next are shown in Fig. 10.

Fig. 11. Simulation of the fluid-mechanical sewing machine. The thread is poured from a constant height onto a moving belt. As the velocity of the belt is increased, the pattern laid out by the thread undergoes a series of bifurcations, similar to those that have been reported in the experiments: for this particular value of the fall height, translated coiling, alternated loops and meanders are successively obtained. Arrows of different lengths indicate the velocity of the belt as the pattern was formed: the belt moves to the right and more ancient patterns, corresponding to a slower belt, are located on the right-hand side. Simulation parameters are the same as in Ref. [13] and are provided in the main text.

6.2. Application to the viscous sewing machine

The fluid-mechanical sewing machine is an extension of the steady coiling problem to the case of a moving substrate [12,13]. To the best of our knowledge, our numerical method is the first one that can simulate this essentially non-steady phenomenon.

Some of us have published in a separate article [42] a detailed analysis of the viscous sewing machine, considered from a fluid-mechanical perspective. A typical simulation is presented in Fig. 11, when the velocity of the belt is steadily increased. The patterns must be read from right to left: this corresponds to the order in which they were produced, and so to an increasing belt velocities. On the right-hand side, for a low belt velocity, the translated coiling pattern is obtained. Increasing the belt velocity, two successive transitions are observed, leading to the formation of alternated loops first, and to meanders next. For even larger belt velocities, the oscillations disappear and the pattern becomes straight (not shown) as the hanging part of the thread takes on a catenary-like shape. The same sequence of patterns has been observed in the experiments, and is typical of small fall heights. A variety of patterns, some of which are quite complex, are obtained at larger fall heights both in the experiments and in the simulations, see Ref. [42] for details.

The parameters used to produce the results of Fig. 11 are the same as in the experiments of Morris [13] but without surface tension ($\gamma = 0$). We use a convenient set of units in which the fluid's dynamical viscosity is $\mu = 1$, its mass density is $\rho = 1$, and the acceleration of gravity is $g = 1$. With this natural set of units, the quantities L^* and T^* defined earlier read $L^* = 1$ and $T^* = 1$. The fall height is fixed to $H = 0.865$; this corresponds to a physical fall height of 3.7 cm in the experiments [13]. The area of the circular outlet at the bottom of the container is set to $A_c = 0.0275$, and the imposed volume flow rate is $Q_c = 2.29 \times 10^{-5}$. The corresponding values of the dimensionless groups read $\Pi_1 = 608.5$, $\Pi_2 = 0.369$, $\Pi_3 = 0$. The belt is held still until time $t_1 = 919$ for the initial transient relax. From this time on, the belt velocity is steadily accelerated until the end of the simulation, occurring at time $t_f = 1650$, its final velocity being 0.02.

The spatial discretization parameter is set to $\ell_c = 0.005$, and the time step to $\epsilon = 0.05$. We handle collisions using the time roll-back method, $c = \texttt{rb}$. The stretching effect of gravity is severe, and the mesh is refined adaptively to maintain a good resolution near the bottom of the thread, as explained in Section 4.5. The subdivision criterion was set up by trial and errors, using the reference steady coiling solution:

$$f(\ell, \ell_0, z) = \big(\ell > \min\big(1.96\ell_0, 0.0062^{\max(0, \frac{z-0.1}{0.02})}\big)\big). \tag{77}$$

It forces subdivision whenever the segments get stretched by a factor close to 2, and whenever they approach the coil region near the floor $z = 0$, where a good resolution is needed. Segments are refined up to the sixth generation in the simulation.

6.3. Limitations and perspectives

The present paper presents a time scheme based on a semi-implicit discretization of the viscous force: this force is treated implicitly with respect to the velocity but explicitly with respect to positions, see Eq. (72). Compared to a fully explicit scheme, this method is more difficult to implement but vastly superior in terms of robustness. In a previous paper, we have explored a fully implicit scheme [41], by retaining the non-linear dependence of the viscous forces on positions: in that case, each time step requires a non-linear root-finding. The benefit of the non-linear implicit approach is that it preserves conservation laws associated with the symmetries of the problem, such as the conservation of the angular momentum, when it applies. By contrast the method presented here displays the usual dissipation of angular momentum. This is a minor drawback as viscous thread are never encountered as free-standing bodies. In all the demonstration examples shown earlier, neither the linear nor the angular momentum of the thread are actually conserved, because of the exchange of momentum with the floor and nozzle during collisions.

In future work, it would be interesting to extend the present numerical model to thin threads governed by more general constitutive laws, such as visco-elastic filaments [48,72] which can exhibit a complex and poorly understood behavior [73]. To this end, the discrete geometrical model exposed in the present paper can be reused and combined with different constitutive laws. It would also be interesting to couple our thin thread model with existing simulation methods for 3d flows with free boundaries [74,75,20,67], in order to capture the interaction of the thread with the slowly collapsing pile that forms where it merges with the bath.

6.4. Conclusion

We have presented a numerical method for simulating the dynamics of thin viscous threads. In contrast with existing numerical methods, it captures the combined effects of stretching, bending and twisting forces, inertia and large rotations. It is not restricted to steady flows. The method has been derived by writing the smooth equations of motion for thin threads into a Lagrangian form, and using a careful spatial discretization. In particular, a discrete notion of twist has been used, which is based on the geometry of parallel transport. The internal stress representing the internal viscous stress has been derived from variational principles, using a Rayleigh potential. All the relevant physical quantities, such as strain rates and internal stress, have been identified in the discrete setting. Our discrete equations are equivalent with the classical smooth equations in the limit of a zero mesh size, as shown in Appendix B. The method has been validated against reference solutions available for steady coiling. Demonstration examples in the non-steady case have been shown.

We would like to thank Neil Ribe for getting us interested into the fascinating dynamics of thin threads, and for sharing his continuation data which enabled us to validate our code.

Acknowledgements

MW acknowledges partial support by the BMBF research project GeoMec. MB and EG were partially supported by the National Science Foundation (CMMI-1129917, IIS-1117257).

Appendix A. Interpretation of the strain rates

We show that the rates of strain defined in the main text are the convected derivatives of the elastic strain. This is consistent with the Rayleigh–Taylor analogy, which states that the viscous constitutive laws are identical to the elastic ones when the strain is replaced with the time derivative of strain.

A.1. Interpretation of the axial stretch rate

The Lagrangian axial strain rate d has been defined in Eq. (10) by $d(S,t) = \underline{t}(S,t) \cdot \underline{u}'(S,t)$. This quantity is equal to the convected derivative of the stretch $\ell(S,t)$ defined in Eq. (7):

$$d(S,t) = \underline{t}(S,t) \cdot \frac{\partial \underline{u}(S,t)}{\partial S} = \frac{1}{\ell}\underline{T} \cdot \frac{\partial \underline{T}}{\partial t} = \frac{1}{2\ell}\frac{\partial (\underline{T}^2)}{\partial t} = \frac{1}{2\ell}\frac{\partial (\ell^2)}{\partial t} = \frac{\partial \ell}{\partial t}. \tag{A.1}$$

Here we have used the identity $\dot{\underline{T}} = \underline{u}'$, that follows from the definitions $\underline{T} = \underline{x}'$ and $\underline{u} = \dot{\underline{x}}$. The right-hand side conforms with our intuition of the strain rate $d(S,t)$ as measuring the rate of stretching of material segments parallel to the centerline.

A.2. Interpretation of the rate of change of twist and curvature

The rotation velocity $\underline{\omega}$ and the twist-curvature vector $\underline{\pi}$ characterize infinitesimal changes of the material frame $\underline{d}_i(S,t)$ corresponding to increments of time t and of arc length S, respectively. A compatibility condition relating the space derivative of $\underline{\omega}'$ and the time derivative of $\dot{\underline{\pi}}$ can be derived as follows. We start from the identity of the cross-derivatives of the material frame vectors, $\partial \underline{d}_i'/\partial t = \partial \dot{\underline{d}}_i/\partial S$. Inserting the definitions of the angular velocity, $\dot{\underline{d}}_i = \underline{\omega} \times \underline{d}_i$ and of the twist-curvature vector, $\underline{d}_i' = \underline{\pi} \times \underline{d}_i$, and eliminating $\underline{d}_i$ we find, after some algebra:

$$\frac{\partial \underline{\omega}}{\partial S} = \frac{\partial \underline{\pi}}{\partial t} - \underline{\omega} \times \underline{\pi},$$

which is also known as the Maurer–Cartan identity.

The right-hand side is the covariant derivative of $\underline{\pi}$, and enjoys the property that it commutes with the longitudinal and perpendicular projections:

$$\frac{\partial \underline{\omega}}{\partial S} \cdot \underline{t} = \frac{\partial (\underline{\pi} \cdot \underline{t})}{\partial t} \tag{A.2a}$$

$$\underline{P}_\perp\left(\underline{t}, \frac{\partial \underline{\omega}}{\partial S}\right) = \frac{\partial \underline{P}_\perp(\underline{t}, \underline{\pi})}{\partial t} - \underline{\omega} \times \underline{P}_\perp(\underline{t}, \underline{\pi}). \tag{A.2b}$$

In the left-hand sides, one can identify the rate of strain $\underline{e} = \underline{\omega}'$ introduced in Eq. (18), whose tangent projection e_t is relevant to the twisting mode, and whose perpendicular projection $\underline{e}_b$ is relevant to the bending mode, by Eqs. (19). The tangent and perpendicular projections of $\underline{\pi}$ are the kinematic twist τ and the binormal curvature $\underline{K}$ by Eq. (17b). Therefore, we can rewrite the above set of equations as

$$e_{\mathrm{t}}(S,t) = \frac{\partial \tau(S,t)}{\partial t} \tag{A.3a}$$

$$\underline{e}_{\mathrm{b}}(S,t) = \frac{\partial \underline{K}(S,t)}{\partial t} - \underline{\omega} \times \underline{K}(S,t). \tag{A.3b}$$

The strain rates are therefore equal to the convected derivative of the kinematic strain τ (twisting mode) and to the convected derivative of the binormal curvature measured in the rotating material frame (bending mode).

Appendix B. Equivalence with Kirchhoff equations

This section establishes the equivalence of the Lagrangian description of threads based on the centerline/spin representation $(\underline{x}, v)$ used in our implementation, and the Kirchhoff equations for thin viscous threads widely used in fluid mechanics. In doing so, we shall identify important quantities, such as the viscous stress. This appendix is not required for the implementation.

B.1. Constitutive laws underlying the Rayleigh potential

To cast our equations into the formalism of Kirchhoff, we shall start by calculating the force $\underline{P}_{\mathrm{v}}$ and twisting moment Q_{v} arising from viscous stress. By Eq. (30), this requires working out the first variation of the Rayleigh potential with respect to the velocities $\hat{\underline{u}}$ and $\hat{v}$, near the real motion $\hat{\underline{u}} = \underline{u} = \dot{\underline{x}}$ and $\hat{v} = v$. By Eqs. (27) and (29), we can write this first variation as

$$-\mathrm{d}\mathcal{D}(\underline{x}; \underline{u}, v; \delta\underline{u}, \delta v) = -\int_{S_-}^{S^+} \left(n_{\mathrm{s}}\, \mathrm{d}\mathcal{L}_{\mathrm{s}}(\delta\underline{u}) + \underline{m} \cdot \mathrm{d}\underline{\mathcal{M}}(\delta\underline{u}, \delta v)\right) \mathrm{d}S, \tag{B.1}$$

where

$$\mathrm{d}\underline{\mathcal{M}}(\underline{x}; \delta\underline{u}, \delta v; S) = \underline{t}(S)\, \mathrm{d}\mathcal{L}^{\mathrm{t}}(\underline{x}; \delta\underline{u}, \delta v; S) + \mathrm{d}\underline{\mathcal{L}}^{\mathrm{b}}(\underline{x}; \delta\underline{u}, \delta v; S). \tag{B.2}$$

The coefficients appearing in this variation have been denoted by n_{s} and $\underline{m}$:

$$n_{\mathrm{s}}(S,t) = \left.\frac{\partial \mathcal{D}_{\mathrm{s}}}{\partial \mathcal{L}_{\mathrm{s}}(S)}\right|_{\mathrm{rm}} = D\frac{\mathcal{L}_{\mathrm{s}}|_{\mathrm{rm}}}{\ell} = D\frac{d}{\ell} \tag{B.3a}$$

$$\underline{m}(S,t) = \left.\frac{\partial \mathcal{D}_{\mathrm{t}}}{\partial \mathcal{L}^{\mathrm{t}}(S)}\right|_{\mathrm{rm}} \underline{t} + \left.\frac{\partial \mathcal{D}_{\mathrm{b}}}{\partial \underline{\mathcal{L}}^{\mathrm{b}}(S)}\right|_{\mathrm{rm}} = C\frac{e_{\mathrm{t}}}{\ell}\underline{t} + B\frac{\underline{e}_{\mathrm{b}}}{\ell}. \tag{B.3b}$$

They depend only on the real motion, as denoted by the subscript 'rm'. In this expressions we have omitted some of the arguments such as $\underline{x}$, $\underline{u}$, v and S for better legibility.

Eqs. (B.3) are the constitutive laws for a viscous thread: B, C and D are the viscous moduli introduced in Eqs. (28), $\underline{m}$ the internal moment arising from twisting and bending, and n_{s} is the scalar tension resisting stretching. The latter gives rise to an internal tension force measured by the *vector*

$$\underline{n}_{\mathrm{s}}(S,t) = n_{\mathrm{s}}(S,t)\underline{t}(S,t). \tag{B.4}$$

When rewritten in terms of the Eulerian rates of strain defined by

$$d^{\mathrm{E}} = \frac{d}{\ell}, \qquad \underline{e}^{\mathrm{E}} = \frac{e_{\mathrm{t}}\,\underline{t} + \underline{e}_{\mathrm{b}}}{\ell} = \frac{\underline{e}}{\ell} = \frac{1}{\ell}\frac{\partial \underline{\omega}}{\partial S} = \frac{\partial \underline{\omega}}{\partial s}, \tag{B.5}$$

Eq. (B.3) yields the classical form of the constitutive laws for a viscous thread: the Trouton law for stretching is $n_{\mathrm{s}} = Dd^{\mathrm{E}}$ and the internal moment associated with twist and bending reads $\underline{m} = [C(\underline{t}\otimes\underline{t}) + B(\underline{\underline{1}} - \underline{t}\otimes\underline{t})]\cdot\underline{e}^{\mathrm{E}}$. Here, the expression in square brackets is known as the tensors of viscous moduli, and the terms in parenthesis are the tangent and perpendicular projections. In Appendix D, we show equivalence with the constitutive laws derived by Ribe [9] from the Stokes equations in 3d.

B.2. Identification of the net viscous force and twisting moment

In Eqs. (19), the rates of strain associated with twist and bending were defined as the longitudinal and perpendicular components of the strain rate vector $\underline{\omega}' = \underline{e}$. In terms of the calligraphic reconstruction operators, this can be written as

$$\frac{\mathrm{d}\underline{\mathcal{W}}(\underline{x}; \hat{\underline{u}}, \hat{v}; S)}{\mathrm{d}S} = \underline{t}(S)\mathcal{L}^{\mathrm{t}}(\underline{x}; \hat{\underline{u}}, \hat{v}; S) + \underline{\mathcal{L}}^{\mathrm{b}}(\underline{x}; \hat{\underline{u}}, \hat{v}; S). \tag{B.6}$$

The right-hand side is linear with respect to the virtual velocities, and as result its first variation with respect to the virtual velocities coincides with the right-hand side of Eq. (B.2). This shows that $\mathrm{d}\underline{\mathcal{M}}$ is equal to the first variation of $\underline{\mathcal{W}}'(S)$. Together with the identity $n_s\,\mathrm{d}\mathcal{L}_s = n_s(\underline{t}\cdot\delta\underline{u}'(S)) = \underline{n}_s\cdot\delta\underline{u}'(S)$, this allows us to rewrite Eq. (B.1) in compact form:

$$-\mathrm{d}\mathcal{D}(\delta\underline{u},\delta v) = -\int_{S_-}^{S^+}\left(\underline{n}_s(S)\cdot\frac{\mathrm{d}[\delta\underline{u}]}{\mathrm{d}S} + \underline{m}(S)\cdot\frac{\mathrm{d}[\mathrm{d}\underline{\mathcal{W}}(\delta\underline{u},\delta v)]}{\mathrm{d}S}\right)\mathrm{d}S. \tag{B.7}$$

Note that for any real motion, the quantity $\underline{\mathcal{W}}$ evaluates to the angular velocity $\underline{\omega}$ by Eq. (22). In the language of the principle of virtual work, the above expression is known as the internal virtual work of thin rods.

We can compute the first variation of $\underline{\mathcal{W}}$, which has been defined earlier in terms of the centerline/spin variables in Eq. (22), as $\mathrm{d}\underline{\mathcal{W}}(\delta\underline{u},\delta v) = \underline{t}\,\delta v + \frac{\underline{t}\times\delta\underline{u}'(S)}{\ell}$. Inserting this into Eq. (B.7), integrating by parts, and identifying the coefficient of δv with Q_v and the coefficient of $\delta\underline{u}$ with $\underline{P}_v$ according to Eq. (30), we find

$$Q_v(S,t) = \frac{\partial\underline{m}(S,t)}{\partial S}\cdot\underline{t}(S,t) \tag{B.8a}$$

$$\underline{P}_v(S,t) = \frac{\partial\underline{n}(S,t)}{\partial S}, \tag{B.8b}$$

where we have defined an auxiliary quantity $\underline{n}(S,t)$, to be interpreted later as the total internal stress resultant:

$$\underline{n}(S,t) = \underline{n}_s(S,t) + \underline{t}(S,t)\times\left(\frac{1}{\ell(S,t)}\frac{\partial\underline{m}(S,t)}{\partial S}\right). \tag{B.8c}$$

In addition to these interior contributions $\underline{P}_v$ and Q_v, the first variation of the Rayleigh potential includes boundary terms that enter into the expression of the viscous forces on the endpoints $S_\pm$: these boundary terms will be considered in the discrete case, as required. These boundary terms yield the same boundary conditions as in the classical Kirchhoff theory, a verification that is left to the interested reader.

B.3. Equivalence with Kirchhoff equations

Dividing the Lagrangian equation of motion (31a) by ℓ and combining with the definition of $\underline{n}$ in Eq. (B.8c), we have

$$\frac{1}{\ell}\frac{\partial\underline{n}(S,t)}{\partial S} + \frac{\underline{P}}{\ell} = \rho\,\frac{A_0}{\ell}\,\ddot{\underline{x}}. \tag{B.9}$$

We recover the first Kirchhoff equation for the balance of linear momentum, usually written $\partial\underline{n}/\partial s + \underline{P}^{\mathrm{E}} = \rho A\,\ddot{\underline{x}}$, after identification of the arclength in actual configuration $\mathrm{d}s = \ell\,\mathrm{d}S$, of the Eulerian density of external load $\underline{P}^{\mathrm{E}} = \underline{P}/\ell$ and of the cross-section area A in actual configuration by Eq. (13).

To establish the second Kirchhoff equation, we note that the transverse and tangent projections of $\frac{\partial\underline{m}}{\partial s} = \frac{1}{\ell}\frac{\partial\underline{m}}{\partial S}$ enter in the definition of $\underline{n}$ in Eq. (B.8c), and in the expression (B.8a) of the net twisting moment Q_v, respectively. Combining with the second equation of motion (31b), this yields

$$\frac{\partial\underline{m}}{\partial s} = -\underline{t}\times\underline{n} + J\dot{v}\underline{t} - \frac{Q}{\ell}\underline{t}. \tag{B.10}$$

We recover the second Kirchhoff equation for the balance of angular momentum, usually written $\partial\underline{m}/\partial s + \underline{t}\times\underline{n} + Q^{\mathrm{E}}\underline{t} = J\dot{v}\underline{t}$, where $Q^{\mathrm{E}} = Q/\ell$ is the Eulerian density of twisting moment applied on the rod. We have therefore established the equivalence of our formalism with the classical, Eulerian equations for thin viscous threads.

Appendix C. Parallel transport, discrete twist

The main difficulty in setting up a discrete model for thin viscous thread resides in the definition of twist. In the smooth case, twist is defined by projecting the infinitesimal rotation vector $\underline{\pi}$ along the tangent. This operation is no longer possible in the discrete case, as rotations are finite and are represented by a matrix. To remedy this difficulty, we define twist by difference with the geometrical notion of parallel transport, which can be extended naturally to the discrete case.

C.1. A geometrical view of twist-less configurations: parallel transport

Consider the unit tangents $\underline{t}^{i-1}$ and $\underline{t}^{i}$ of the segments adjacent to a vertex $\underline{x}_i$. We shall assume that these tangents are not opposite to each other,

$$\underline{t}^{i-1} \neq -\underline{t}^{i}. \tag{C.1}$$

This assumption is satisfied, except for a subset of configurations whose measure is zero, which we ignore. A rotation matrix $\underline{\underline{Q}}$ is said to be *compatible* at vertex $\underline{x}_i$ if it maps $\underline{t}^{i-1}$ to $\underline{t}^i$:

$$\underline{\underline{Q}} \cdot \underline{t}^{i-1} = \underline{t}^i. \tag{C.2}$$

Given two unit tangents $\underline{t}^{i-1}$ and $\underline{t}^i$ subjected to the condition (C.1), we define parallel transport across vertex $\underline{x}_i$ as *the minimal rotation that is compatible*, in the sense of Eq. (C.2). Here, 'minimal' refers to the rotation having the smallest possible angle of rotation about its own axis.[1] This defines a unique rotation under the assumption of Eq. (C.1), as we show below. In the smooth case, parallel transport is related to Bishop's notion of natural frame on a curve [76,57].

Equivalently, parallel transport can be defined as the rotation $\underline{\underline{T}}_i$ whose axis is along the binormal $\underline{K}_i$ and whose angle is the turning angle φ_i across vertex $\underline{x}_i$. The turning angle is defined by

$$\varphi_i = \cos^{-1}\big(\underline{t}^{i-1} \cdot \underline{t}^i\big) \quad \text{with } 0 \leqslant \varphi_i < \pi. \tag{C.3}$$

Note that $\varphi_i \neq \pi$ by Eq. (C.1). The rotation $\underline{\underline{T}}_i$ just defined satisfies

$$\underline{\underline{T}}_i^T \cdot \underline{\underline{T}}_i = \underline{\underline{1}} \tag{C.4a}$$

$$\underline{\underline{T}}_i \cdot \underline{K}_i = \underline{K}_i \tag{C.4b}$$

$$\underline{\underline{T}}_i \cdot \underline{t}^{i-1} = \underline{t}^i. \tag{C.4c}$$

Indeed, $\underline{\underline{T}}_i$ is a rotation, its axis is aligned with the binormal curvature $\underline{K}_i$, and its rotation angle φ_i is such that it is compatible. In the particular case where the adjacent segments are aligned, $\underline{t}^{i-1} = \underline{t}^i$, we have $\varphi_i = 0$ and parallel transport is the identity matrix:

$$\underline{\underline{T}}_i = \underline{\underline{1}} \quad \text{if } \varphi_i = 0. \tag{C.4d}$$

Any compatible rotation maps $\underline{t}^{i-1}$ to $\underline{t}^i$, and as a consequence its angle of rotation has to be greater or equal to the angle φ_i between them. The angle of rotation of the matrix $\underline{\underline{T}}_i$ that we have just defined is precisely φ_i. This almost establishes the equivalence of the geometrical and practical definitions of parallel transport; to complete the proof, we have to show that the there is a unique compatible rotation whose rotation angle is equal to φ_i. This is what we do now.

First note that any compatible rotation $\underline{\underline{Q}}$ can be decomposed as

$$\underline{\underline{Q}} = \underline{\underline{T}}_i \cdot \underline{\underline{R}}\big(\underline{t}^{i-1}, \tau(\underline{\underline{Q}})\big) \tag{C.5}$$

for some angle $\tau(\underline{\underline{Q}})$. Here $\underline{\underline{R}}(\underline{t}^{i-1}, \tau)$ denotes the rotation about $\underline{t}^{i-1}$ with angle τ. This decomposition follows from the remark that $\underline{\underline{T}}_i^{-1} \cdot \underline{\underline{Q}}$ is a rotation leaving $\underline{t}^{i-1}$ invariant. Denoting $\underline{q}_\sigma$ the unit vector obtained by rotating $\underline{t}^{i-1}$ about the binormal by an angle σ, one can compute the scalar product of $\underline{q}_\sigma$ with its image $\underline{q}'_\sigma = \underline{\underline{Q}} \cdot \underline{q}_\sigma$ as

$$\underline{q}_\sigma \cdot \underline{q}'_\sigma = \cos\varphi_i + \big[\sin(\varphi_i - \sigma)\sin(\sigma)\big]\big(1 - \cos\tau(\underline{\underline{Q}})\big). \tag{C.6}$$

This equality can be established in the direct orthonormal basis whose first and last vectors are $\underline{t}^{i-1}$ and $\underline{K}_i/|\underline{K}_i|$, respectively; in this frame, $\underline{q}_\sigma = \{\cos\sigma, \sin\sigma, 0\}$ and $\underline{t}^i = \{\cos\varphi_i, \sin\varphi_i, 0\}$. Details of the calculation are left to the reader.

Being obtained one from each other by a rotation with angle φ_i, the unit vectors $\underline{q}_\sigma$ and $\underline{q}'_\sigma$ make an angle smaller than φ_i, and so, $\underline{q}_\sigma \cdot \underline{q}'_\sigma \geqslant \cos\varphi_i$ for any σ. By the equation above, $[\sin(\varphi_i - \sigma)\sin(\sigma)](1 - \cos\tau(\underline{\underline{Q}})) \geqslant 0$. Assuming $\varphi_0 \neq 0$, there exists at least a value of σ that makes the square bracket of Eq. (C.6) negative and non-zero; this shows that $\tau(\underline{\underline{Q}}) = 0$ in Eq. (C.5) and so $\underline{\underline{Q}} = \underline{\underline{T}}_i$, as announced. The case $\varphi_0 = 0$ is trivial, as the identity mapping is obviously the minimal rotation (its angle is zero) leaving $\underline{t}^{i-1} = \underline{t}^i$ invariant. We have just shown that there is a unique compatible rotation whose angle is minimal, and this defines the parallel transport $\underline{\underline{T}}_i$.

Parallel transport establishes a natural mapping between cross-sections belonging to neighboring segments, and is similar to the notion of a Levi-Civita connection in the smooth case [77]. It is used to define the discrete twist by difference: twist-less configurations of the rod to be those obtained by parallel-transporting the material frames from one segment to the next.

In the smooth case, the identification of parallel transport with twist-less configurations of the rod can be justified as follows. Infinitesimal compatible rotations of a frame compatible with a prescribed curve are associated with a Darboux vector $\underline{\pi} = \underline{K} + \tau\underline{t}$ by Eq. (17b). The binormal curvature $\underline{K}$ is a function of the curve. Minimizing the rate of rotation $|\underline{\pi}|$ while holding the curve fixed leads to $\tau(S,t) = 0$, which indeed characterizes twist-less configurations.

[1] In geometrical terms, this minimal rotation minimizes the distance to the identity over the Lie group of direct rotations in Euclidean 3d space.

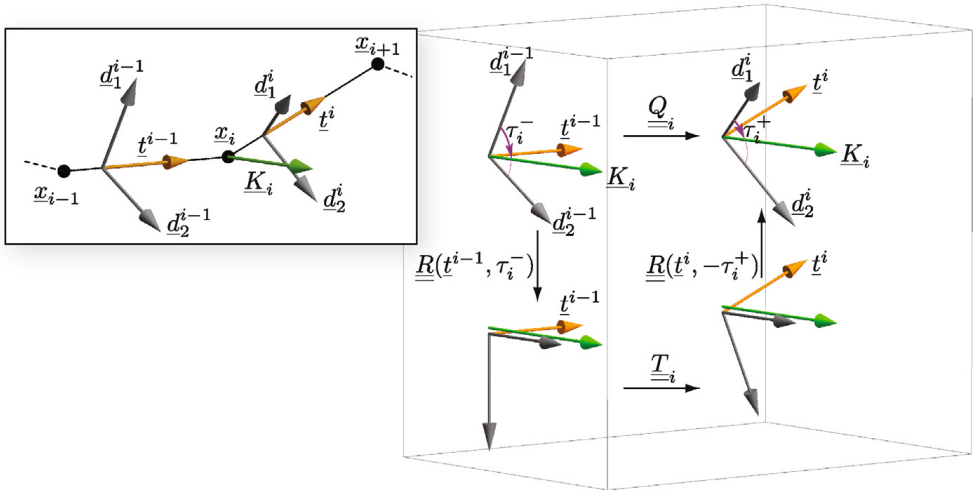

Fig. 12. Notations used for computing the rate of change of the discrete twist, and illustration of Eq. (C.10). The rotation mapping one material frame to the next is decomposed using parallel transport and the polar angles τ_i^- and τ_i^+.

C.2. Discrete twist of a framed curve

Recall that material frames are orthonormal. Let then $\underline{\underline{Q}}_i$ be the unique rotation mapping one material frame to the next:

$$\underline{d}_j^i = \underline{\underline{Q}}_i \cdot \underline{d}_j^{i-1} \quad \text{for } j = 1, 2, 3. \tag{C.7}$$

This rotation is compatible, as $j = 3$ yields Eq. (C.2) again after using the adaptation condition (48). Using a similar decomposition as earlier in Eq. (C.5), there exists an angle $\tau_i = \tau(\underline{\underline{Q}}_i)$ such that

$$\underline{\underline{Q}}_i = \underline{\underline{T}}_i \cdot \underline{\underline{R}}\big(\underline{t}^{i-1}, \tau_i\big) = \underline{\underline{R}}\big(\underline{t}^i, \tau_i\big) \cdot \underline{\underline{T}}_i. \tag{C.8}$$

The second equality follows from the fact that the rotation $[\underline{\underline{T}}_i \cdot \underline{\underline{R}}(\underline{t}^{i-1}, \tau_i) \cdot \underline{\underline{T}}_i^T]$ is conjugate to $\underline{\underline{R}}(\underline{t}^{i-1}, \tau_i)$, and so has the angle of rotation τ_i, and leaves $\underline{t}^i$ invariant; it is therefore the rotation about $\underline{t}^i$ with angle τ_i, which is noted $\underline{\underline{R}}(\underline{t}^i, \tau_i)$. Note that the angle τ_i is uniquely defined modulo 2π.

The angle τ_i defines the axial rotation required to make neighboring material frames coincide, in complement with parallel transport $\underline{\underline{T}}_i$. It is called the discrete angle of twist across the vertex $\underline{x}_i$. Note that the rotations $\underline{\underline{Q}}_i$, $\underline{\underline{T}}_i$ and $\underline{\underline{R}}(\underline{t}^i, \tau_i)$ converge in the smooth limit towards infinitesimal rotations represented by Darboux vectors $\underline{\pi}$, $\underline{K}$ and $\tau_i \underline{t}$ respectively; in this limit, Eq. (C.8) becomes $\underline{\pi} = \underline{K} + \tau_i \underline{t}$, and we recover Eq. (17b). This confirms that our definition of the discrete twist is consistent in the smooth limit.

C.3. Rate of change of twist

In Section 3.4, the rate of twisting strain is defined as the time derivative $\dot{\tau}_i$ of the twist angle. Here, we work out its expression in terms of the centerline/spin variables. Let us tart by introducing the polar angles τ_i^- and τ_i^+ of the binormal $\underline{K}_i$ in the frames $(\underline{d}_1^{i-1}, \underline{d}_2^{i-1})$ and $(\underline{d}_1^i, \underline{d}_2^i)$, respectively, as shown in Fig. 12. They can be computed by taking the arctangent of the coordinates of the vector $\underline{t}^{i-1} \times \underline{t}^i$, which is aligned with $\underline{K}_i$ by definition of the latter. These coordinates are denoted by $(\tau_{i1}^-, \tau_{i2}^-)$ in the first frame and $(\tau_{i1}^+, \tau_{i2}^+)$ in the second frame:

$$\tau_i^\pm = \tan^{-1}\left(\frac{\tau_{i2}^\pm}{\tau_{i1}^\pm}\right), \tag{C.9a}$$

where

$$\tau_{ij}^\pm = \big(\underline{t}^{i-1} \times \underline{t}^i\big) \cdot \underline{d}_j^{i+(\pm 1-1)/2}. \tag{C.9b}$$

In the second equation, j takes on the values 1 or 2, and the superscript in the last factor evaluates to the index $(i-1)$ of the segment in the left-hand side when $\pm = -$, and to the index (i) of the segment in the right-hand side when $\pm = +$.

As shown graphically in Fig. 12, the rotation $\underline{\underline{Q}}_i$ can be decomposed into a rotation about $\underline{t}^{i-1}$ with angle τ_i^- that brings $\underline{d}_1^{i-1}$ onto the binormal $\underline{K}_i$, composed by the parallel transport that maps $\underline{t}^{i-1}$ to $\underline{t}^i$ without affecting the binormal,

and composed by another rotation about $\underline{t}^i$ with angle $(-\tau_i^+)$ that brings back the binormal to $\underline{d}_1^i$ without affecting the tangent:

$$\underline{\underline{Q}}_i = \underline{\underline{R}}\big(\underline{t}^i, -\tau_i^+\big) \cdot \underline{\underline{T}}_i \cdot \underline{\underline{R}}\big(\underline{t}^{i-1}, \tau_i^-\big). \tag{C.10}$$

As earlier in Eq. (C.8), we can use conjugation to group the axial rotations in equation above. Identifying the result with the definition of τ_i in Eq. (C.8), we have $\tau_i = \tau_i^- - \tau_i^+$. Our aim is to compute is the quantity

$$\dot\tau_i = \dot\tau_i^- - \dot\tau_i^+. \tag{C.11}$$

To derive an expression for $\dot\tau_i^\pm$, we first compute $\dot\tau_{ij}^-$ in the frame moving with the first material frame $(d_j^{i-1})_{1\leqslant j\leqslant 3}$. In this frame, all vectors in the right-hand side of Eq. (C.9b) are still, except $\underline{t}^i$ which has angular velocity $\underline{\omega}^i - \underline{\omega}^{i-1}$. This yields, for $j = 1, 2$,

$$\dot\tau_{ij}^- = \big(\underline{t}^{i-1} \times \big[\big(\underline{\omega}^i - \underline{\omega}^{i-1}\big) \times \underline{t}^i\big]\big) \cdot \underline{d}_j^{i-1} = -\big(\underline{t}^{i-1} \times \underline{d}_j^{i-1}\big) \cdot \big[\big(\underline{\omega}^i - \underline{\omega}^{i-1}\big) \times \underline{t}^i\big],$$

after permutation of the mixed product. Inserting this expression into the derivative of the arctangent in Eq. (C.9a), we find

$$\dot\tau_i^- = \frac{\tau_{i1}^-\,\dot\tau_{i2}^- - \tau_{i2}^-\,\dot\tau_{i1}^-}{(\tau_{i1}^-)^2 + (\tau_{i2}^-)^2} = \frac{(\underline{t}^{i-1} \times \underline{t}^i) \cdot [(\underline{\omega}^i - \underline{\omega}^{i-1}) \times \underline{t}^i]}{|\underline{t}^{i-1} \times \underline{t}^i|^2}. \tag{C.12a}$$

The time derivative of the second angle τ_i^+ is given by the same formula, with the indices i and $i-1$ swapped:

$$\dot\tau_i^+ = \frac{(\underline{t}^{i-1} \times \underline{t}^i) \cdot [(\underline{\omega}^i - \underline{\omega}^{i-1}) \times \underline{t}^{i-1}]}{|\underline{t}^{i-1} \times \underline{t}^i|^2}. \tag{C.12b}$$

Inserting this expression into Eq. (C.11) and permuting the mixed product, we have

$$\dot\tau_i = \big(\underline{\omega}^i - \underline{\omega}^{i-1}\big) \cdot \frac{(\underline{t}^i - \underline{t}^{i-1}) \times (\underline{t}^{i-1} \times \underline{t}^i)}{|\underline{t}^{i-1} \times \underline{t}^i|^2}. \tag{C.13}$$

In the right-hand side, the second factor can be simplified using the fact that both $\underline{t}^{i-1}$ and $\underline{t}^i$ are unit vectors. This yields

$$\dot\tau_i = \big(\underline{\omega}^i - \underline{\omega}^{i-1}\big) \cdot \frac{\underline{t}^{i-1} + \underline{t}^i}{1 + \underline{t}^{i-1} \cdot \underline{t}^i},$$

in close analogy with the smooth equation (19a). Inserting now the decomposition (49) of the material velocity $\underline{\omega}^j$ and simplifying, we have

$$\dot\tau_i = v^i - v^{i-1} + \underline{K}_i \cdot \frac{\dot{\underline{t}}^{i-1} + \dot{\underline{t}}^i}{2}, \tag{C.14}$$

after using the definition (45) of the discrete binormal curvature $\underline{K}_i$.

Eq. (C.14) is used in the code to compute the rate of twisting strain. Like its smooth counterpart, see Eq. (24), it captures the geometrical coupling between the mode of rotation and the centerline motion. The geometrical origin of this coupling has been recognized earlier but has not been used as a starting point for dynamical simulations of threads, to the best of our knowledge. The role of the binormal curvature $\underline{K}$ has been noted in the related context of Füller's theorem [55] that yields the increment of writhe of a space curve. Expressions similar to those in Eqs. (C.12) have been derived for the increment of discrete writhe, and have been used for the simulation of the Brownian dynamics of DNA modeled as an elastic rod [78].

Appendix D. Equivalence with the constitutive equations of Ribe

In a classical paper, Ribe analyzed the helical coiling of viscous jets falling on a plane [9]. In the frame rotating with the jet, the shape of the centerline is stationary. The equations for the shape of the jet are expressed as a set of non-linear ordinary differential equations with boundary conditions at both ends. This non-linear boundary-value problem was solved by numerical continuation techniques, using the AUTO [70] software. These solutions, which corresponds to steady configurations, have been used to validate our dynamical code. We show below that our constitutive laws are equivalent to those derived by Ribe from the Stokes equations in 3d.

Ribe introduces an Eulerian twist-curvature vector $\underline{\pi}^{\mathrm{E}}$ which satisfies an equation similar to our Eq. (14b), but with a derivative with respect to arc length s in actual configuration:

$$\frac{\partial \underline{d}_i}{\partial s} = \underline{\pi}^{\mathrm{E}} \times \underline{d}_i. \tag{D.1}$$

The components of $\underline{\pi}^{\mathrm{E}}$ are denoted by

$$\underline{\pi}^{\mathrm{E}} = \begin{bmatrix} \kappa_1 \\ \kappa_2 \\ \kappa_3 \end{bmatrix}, \tag{D.2}$$

where the square brackets indicate a decomposition in the material frame $(\underline{d}_1, \underline{d}_2, \underline{d}_3)$, which is a 'moving' frame, *i.e.* this frame varies with the arc length parameter.

As in Eq. (17b), the Eulerian kinematic twist τ^{E} and binormal curvature vector $\underline{K}^{\mathrm{E}}$ are obtained by a decomposition of the twist-curvature vector $\underline{\pi}^{\mathrm{E}}$ into transverse and tangential components,

$$\tau^{\mathrm{E}} = \kappa_3, \qquad \underline{K}^{\mathrm{E}} = \begin{bmatrix} \kappa_1 \\ \kappa_2 \\ 0 \end{bmatrix}. \tag{D.3}$$

In the frame rotating with the coils, the material rotation $\underline{\omega}_{\mathrm{R}}$ is written in a way that is similar to Eq. (17a), $\underline{\omega}_{\mathrm{R}} = \underline{t} \times \dot{\underline{t}}_{\mathrm{R}} + \omega_3 \underline{d}_3$, where $\dot{\underline{t}}_{\mathrm{R}}$ is the time derivative evaluated in the rotating frame. Since the shape of the thread is steady in this frame, we have $\dot{\underline{t}}_{\mathrm{R}} = U \frac{\partial \underline{\omega}_{\mathrm{R}}}{\partial s} = U \underline{\pi}^{\mathrm{E}} \times \underline{t}$, where $U = \underline{u}_{\mathrm{R}} \cdot \underline{t}$ is the axial velocity of the fluid in the rotating frame. The expression for the material angular velocity can be obtained by combining the above equations,

$$\underline{\omega}_{\mathrm{R}} = \begin{bmatrix} U\kappa_1 \\ U\kappa_2 \\ \omega_3 \end{bmatrix}. \tag{D.4}$$

The material angular velocity in the laboratory frame follows from the composition of velocities, that is $\underline{\omega} = \underline{\omega}_{\mathrm{R}} + \Omega \underline{e}_z$ where Ω is the frequency of coiling, which coincides with the relative angular velocity of the rotating frame with respect to the laboratory, and $\underline{e}_z$ is the axis of rotation of the coils.

As a result, the Eulerian gradient of rotation reads

$$\frac{\partial \underline{\omega}}{\partial s} = \frac{\partial}{\partial s} \begin{bmatrix} U\kappa_1 \\ U\kappa_2 \\ \omega_3 \end{bmatrix} = \begin{bmatrix} (U\kappa_1)' \\ (U\kappa_2)' \\ \omega_3' \end{bmatrix} + \underline{\pi}^{\mathrm{E}} \times \begin{bmatrix} U\kappa_1 \\ U\kappa_2 \\ \omega_3 \end{bmatrix} = \begin{bmatrix} (U\kappa_1)' + \kappa_2(\omega_3 - U\kappa_3) \\ (U\kappa_2)' - \kappa_3(\omega_3 - U\kappa_3) \\ \omega_3' \end{bmatrix}.$$

Here, the term proportional to $\underline{\pi}^{\mathrm{E}}$ comes from the fact that the material frame associated with the square brackets is a moving frame by Eq. (D.1).

These expressions coincide with the rates of strain used by Ribe in his constitutive laws for twisting and bending. This is consistent with our Appendix B.1, and with Eq. (B.5) in particular.

References

[1] M.G. Forest, H. Zhou, Unsteady analyses of thermal glass fibre drawing processes, European Journal of Applied Mathematics 12 (2001) 479–496.
[2] J.R.A. Pearson, Mechanics of Polymer Processing, Applied Science Publishers, New York, NY, USA, 1985.
[3] E. Andreassen, E. Gunderson, E.L. Hinrichsen, H.P. Langtangen, A mathematical model for the melt spinning of polymer fibers, in: M. Daehlem, A. Tveito (Eds.), Numerical Methods and Software Tools in Industrial Mathematics, Birkhäuser, Boston, 1997, pp. 195–212.
[4] D. Shimozuru, Physical parameters governing the formation of Pele hair and tears, Bulletin of Volcanology 56 (3) (1994) 217–219.
[5] A. Herczynski, C. Cernuschi, L. Mahadevan, Painting with drops, jets, and sheets, Physics Today 31 (31) (2011) 32–36.
[6] G. Barnes, R. Woodcock, Liquid rope-coil effect, American Journal of Physics 26 (1958) 205–209.
[7] G.I. Taylor, Instability of jets, threads, and sheets of viscous fluid, in: Proceedings of the 12th International Congress on Applied Mechanics, Stanford, Springer, 1968, p. 382.
[8] L. Mahadevan, W.S. Ryu, A.D.T. Samuel, Fluid 'rope trick' investigated, Nature 392 (140) (1998) 502.
[9] N.M. Ribe, Coiling of viscous jets, Proceedings of the Royal Society A: Mathematical, Physical and Engineering Sciences 460 (2051) (2004) 3223–3239.
[10] N.M. Ribe, H.E. Huppert, M.A. Hallworth, M. Habibi, D. Bonn, Multiple coexisting states of liquid rope coiling, Journal of Fluid Mechanics 555 (1) (2006) 275–297.
[11] N.M. Ribe, M. Habibi, D. Bonn, Stability of liquid rope coiling, Physics of Fluids 18 (8) (2006) 084102.
[12] S. Chiu-Webster, J.R. Lister, The fall of a viscous thread onto a moving surface: a 'fluid-mechanical sewing machine', Journal of Fluid Mechanics 569 (2006) 89–111.
[13] S.W. Morris, J.H.P. Dawes, N.M. Ribe, J.R. Lister, Meandering instability of a viscous thread, Physical Review E (Statistical, Nonlinear, and Soft Matter Physics) 77 (6) (2008) 066218.
[14] F.R.S. Trouton, On the coefficient of viscous traction and its relation to that of viscosity, Proceedings of the Royal Society of London, A 77 (1906) 426–440.
[15] J.D. Buckmaster, A. Nachman, L. Ting, The buckling and stretching of a viscida, Journal of Fluid Mechanics 69 (01) (1975) 1–20.
[16] C.W. Hirt, J.P. Shannon, Free-surface stress conditions for incompressible-flow calculations, Journal of Computational Physics 2 (1968) 403–441.
[17] B.D. Nichols, C.W. Hirt, Improved free surface boundary conditions for numerical incompressible-flow calculations, Journal of Computational Physics 8 (1971) 434–448.
[18] M.F. Tome, S. McKee, GENSMAC: A computational marker and cell method for free surface flows in general domains, Journal of Computational Physics 110 (1) (1994) 171–186.
[19] M.F. Tome, S. McKee, Numerical simulation of viscous flow: Buckling of planar jets, International Journal for Numerical Methods in Fluids 29 (1999) 705–718.

[20] C.M. Oishi, M.F. Tomé, J.A. Cuminato, S. McKee, An implicit technique for solving 3D low Reynolds number moving free surface flows, Journal of Computational Physics 227 (16) (2008) 7446–7468.
[21] W. Arne, N. Marheineke, A. Meister, R. Wegener, Numerical analysis of Cosserat rod and string models for viscous jets in rotational spinning processes, Mathematical Models and Methods in Applied Sciences 11 (20) (2013).
[22] N. Marheineke, R. Wegener, Asymptotic model for the dynamics of curved viscous fibres with surface tension, Journal of Fluid Mechanics 622 (2009) 345–369.
[23] M. Skorobogatiy, L. Mahadevan, Folding of viscous sheets and filaments, Europhysics Letters 52 (5) (2000) 532–538.
[24] N.M. Ribe, Periodic folding of viscous sheets, Physical Review E (Statistical, Nonlinear, and Soft Matter Physics) 68 (3) (2003) 036305.
[25] M.J. Blount, J.R. Lister, The asymptotic structure of a slender dragged viscous thread, Journal of Fluid Mechanics 674 (2011) 489–521.
[26] M. Habibi, Y. Rahmani, D. Bonn, N.M. Ribe, Buckling of liquid columns, Physical Review Letters 104 (2010) 074301.
[27] M. Habibi, P.C.F. Møller, N.M. Ribe, D. Bonn, Spontaneous generation of spiral waves by a hydrodynamic instability, Europhysics Letters 81 (2008) 38004.
[28] J.H. Maddocks, D.J. Dichmann, Conservation laws in the dynamics of rods, Journal of elasticity 34 (1994) 83–96.
[29] A. Goriely, M. Tabor, New amplitude equations for thin elastic rods, Physical Review Letters 77 (17) (1996) 3537–3540.
[30] A. Goriely, M. Tabor, Nonlinear dynamics of filaments II. Nonlinear analysis, Physica D: Nonlinear Phenomena 105 (1–3) (1997) 45–61.
[31] N. Clauvelin, B. Audoly, S. Neukirch, Matched asymptotic expansions for twisted elastic knots: a self-contact problem with non-trivial contact topology, Journal of the Mechanics and Physics of Solids 57 (2009) 1623–1656.
[32] T.Y. Hou, I. Klapper, H. Si, Removing the stiffness of curvature in computing 3-D filaments, Journal of Computational Physics 143 (2) (1998) 628–664.
[33] H. Weiss, Dynamics of geometrically nonlinear rods: II – Numerical methods and computational examples, Nonlinear Dynamics 30 (2002) 383–415.
[34] S. Goyal, N.C. Perkins, C.L. Lee, Nonlinear dynamics and loop formation in Kirchhoff rods with implications to the mechanics of DNA and cables, Journal of Computational Physics 209 (1) (2005) 371–389.
[35] M. Bergou, M. Wardetzky, S. Robinson, B. Audoly, E. Grinspun, Discrete elastic rods, ACM Transactions on Graphics 27 (3) (2008) 63.
[36] S. Lim, A. Ferent, X.S. Wang, C.S. Peskin, Dynamics of a closed rod with twist and bend in fluid, SIAM Journal on Scientific Computing 31 (1) (2008) 273–302.
[37] P. Jung, S. Leyendecker, J. Linn, M. Ortiz, A discrete mechanics approach to Cosserat rod theory. Part 1: Static equilibria, International Journal for Numerical Methods in Engineering (2013).
[38] T.B. Benjamin, T. Mullin, Buckling instabilities in layers of viscous liquid subjected to shearing, Journal of Fluid Mechanics 195 (1988) 523–540.
[39] R. da Silveira, S. Chaïeb, L. Mahadevan, Rippling instability of a collapsing bubble, Science 287 (2013).
[40] R. Radovitzky, M. Ortiz, Error estimation and adaptive meshing in strongly nonlinear dynamic problems, Computer Methods in Applied Mechanics and Engineering 172 (1999) 203–240.
[41] M. Bergou, B. Audoly, E. Vouga, M. Wardetzky, E. Grinspun, Discrete viscous threads, Transactions on Graphics 29 (4) (2010) 116.
[42] P.-T. Brun, N.M. Ribe, B. Audoly, A numerical investigation of the fluid mechanical sewing machine, Physics of Fluids 24 (4) (2012) 043102.
[43] V.M. Entov, A.L. Yarin, The dynamics of thin liquid jets in air, Journal of Fluid Mechanics 140 (1984) 91–111.
[44] J. Buckmaster, The buckling of thin viscous jets, Journal of Fluid Mechanics 61 (3) (1973) 449–463.
[45] J.D. Buckmaster, A. Nachman, The buckling and stretching of a viscida II. Effects of surface tension, The Quarterly Journal of Mechanics and Applied Mathematics 31 (2) (1978) 157–168.
[46] S. Panda, N. Marheineke, R. Wegener, Systematic derivation of an asymptotic model for the dynamics of curved viscous fibers, Mathematical Methods in the Applied Sciences 31 (10) (2008) 1153–1173.
[47] S.E. Bechtel, M.G. Forest, D.B. Bogy, A one-dimensional theory for viscoelastic fluid jets, with application to extrudate swell and draw-down under gravity, Journal of Non-Newtonian Fluid Mechanics 21 (3) (1986) 273–308.
[48] S.E. Bechtel, J.Z. Cao, M.G. Forest, Practical application of a higher order perturbation theory for slender viscoelastic jets and fibers, Journal of Non-Newtonian Fluid Mechanics 41 (3) (1992) 201–273.
[49] Q.-S. Nguyen, Stability and Nonlinear Solid Mechanics, John Wiley & Sons Ltd., 2000.
[50] B. Audoly, Y. Pomeau, Elasticity and Geometry: From Hair Curls to the Nonlinear Response of Shells, Oxford University Press, 2010.
[51] G. Călugăreanu, L'intégrale de Gauss et l'anlyse des nœuds tridimensionnels, Revue de Mathématiques Pures et Appliquées 4 (5) (1959) 5–20.
[52] W. Pohl, The self-linking number of a closed space curve, Indiana University Mathematics Journal 17 (1968) 975–985.
[53] J.H. White, Self-linking and the Gauss integral in higher dimensions, American Journal of Mathematics 91 (3) (1969) 693–728.
[54] F.B. Fuller, The writhing number of a space curve, PNAS 68 (4) (1971) 815–819.
[55] F.B. Fuller, Decomposition of the linking number of a closed ribbon: a problem from molecular biology, PNAS 75 (8) (1978) 3557–3561.
[56] J. Aldinger, I. Klapper, M. Tabor, Formulae for the calculation and estimation of writhe, Journal of Knot Theory and Its Ramification 4 (3) (1995) 343–372.
[57] J. Langer, D.A. Singer, Lagrangian aspects of the Kirchhoff elastic rod, SIAM Review 38 (4) (1996) 605–618.
[58] F. Tanaka, H. Takahashi, Elastic theory of supercoiled DNA, The Journal of Chemical Physics 83 (11) (1985) 6017.
[59] J.H. White, W.R. Bauer, Calculation of the twist and the writhe for representative models of DNA, Journal of Molecular Biology 189 (2) (1986) 329–341, http://dx.doi.org/10.1016/0022-2836(86)90513-9.
[60] I. Tobias, B.D. Coleman, W.K. Olson, The dependence of DNA tertiary structure on end conditions: Theory and implications for topological transitions, The Journal of Chemical Physics 101 (12) (1994) 10990–10996.
[61] K. Klenin, J. Langowski, Computation of writhe in modeling of supercoiled DNA, Biopolymers 54 (5) (2000) 307–317.
[62] A.C. Maggs, Writhing geometry at finite temperature: Random walks and geometric phases for stiff polymers, The Journal of Chemical Physics 114 (13) (2001) 5888–5896, http://dx.doi.org/10.1063/1.1353545.
[63] R.E. Goldstein, T.R. Powers, C.H. Wiggins, Viscous nonlinear dynamics of twist and writhe, Physical Review Letters 80 (23) (1998) 5232–5235.
[64] C.W. Wolgemuth, T.R. Powers, R.E. Goldstein, Twirling and whirling: Viscous dynamics of rotating elastic filaments, Physical Review Letters 84 (7) (2000) 1623–1626.
[65] M. Levitt, Protein folding by restrained energy minimization and molecular dynamics, Journal of Molecular Biology 170 (3) (1983) 723–764.
[66] B. Torby, Advanced Dynamics for Engineers, HRW Series in Mechanical Engineering, Holt Rinehart and Winston, 1984.
[67] C. Batty, R. Bridson, Accurate viscous free surfaces for buckling, coiling, and rotating liquids, in: Proceedings of the 2008 ACM/Eurographics Symposium on Computer Animation, 2008, pp. 219–228.
[68] A.L. Yarin, Free Liquid Jets and Films: Hydrodynamics and Rheology, Longman, New York, NY, 1993.
[69] M.A. Otaduy, R. Tamstorf, D. Steinemann, M. Gross, Implicit contact handling for deformable objects, Computer Graphics Forum 28 (2) (2009) 559–568.
[70] E. Doedel, A.R. Champneys, T.F. Fairgrieve, Y.A. Kuznetsov, B. Sandstede, X.J. Wang, AUTO97: continuation and bifurcation software for ordinary differential equations, available at http://indy.cs.concordia.ca/auto/, 2002.
[71] N.M. Ribe, M. Habibi, D. Bonn, Liquid rope coiling, Annual Review of Fluid Mechanics 44 (2012) 249–266.
[72] H. Tabuteau, S. Mora, G. Porte, M. Abkarian, C. Ligoure, Microscopic mechanisms of the brittleness of viscoelastic fluids, Physical Review Letters 102 (15) (2009) 155501.
[73] T.S. Majmudar, M. Varagnat, W. Hartt, G.H. McKinley, Nonlinear dynamics of coiling in viscoelastic jets, preprint, arXiv:1012.2135v1, 2010.

[74] A. Bonito, M. Picasso, M. Laso, Numerical simulation of 3D viscoelastic flows with free surfaces, Journal of Computational Physics 215 (2) (2006) 691–716.
[75] A. Rafiee, M.T. Manzari, M. Hosseini, An incompressible SPH method for simulation of unsteady viscoelastic free-surface flows, International Journal of Non-Linear Mechanics 42 (10) (2007) 1210–1223.
[76] R. Bishop, There is more than one way to frame a curve, The American Mathematical Monthly 83 (1975) 246–251.
[77] R.M. Wald, General Relativity, University of Chicago Press, 1984.
[78] R. de Vries, Evaluating changes of writhe in computer simulations of supercoiled DNA, The Journal of Chemical Physics 122 (2005) 064905.